Improvement of the longitudinal aerodynamic model for general aviation aircraft with downwash and ground effect models

Vuković, Magdalena

UNIVERSITY OF ZAGREB
FACULTY OF MECHANICAL ENGINEERING
AND NAVAL ARCHITECTURE

MASTER'S THESIS

Magdalena Vuković

Zagreb, 2024.

UNIVERSITY OF ZAGREB
FACULTY OF MECHANICAL ENGINEERING
AND NAVAL ARCHITECTURE

MASTER'S THESIS

Mentors:

Prof. dr. sc. Milan Vrdoljak
Prof. Pierluigi Capone

Student:

Magdalena Vuković

Zagreb, 2024.

I declare that I have completed this thesis independently, using the knowledge acquired during my studies and the referenced literature.

I would like to express my heartfelt gratitude to my mentor prof.dr.sc. Milan Vrdoljak, who organized the opportunity for me to work on this project at ZHAW. My sincere thanks also go to my supervisors at ZHAW, prof. Pierluigi Capone and Noé Pedrazzini, whose previous work formed the foundation of this thesis and whose guidance and expertise were invaluable throughout the project.

I am especially grateful to Jan Juraj Đeverlija for his assistance in running the simulations and to Tobias Zihlmann and Marco Caglioti for serving as test pilots and helping me test my model on the flight simulator. Their contributions were crucial to the success of this work.

Lastly, I would like to thank my family for their unwavering support throughout my education and for making this incredible experience in Switzerland possible. Their encouragement and belief in me have been a source of strength throughout this journey.

Magdalena Vuković

SVEUČILIŠTE U ZAGREBU
FAKULTET STROJARSTVA I BRODOGRADNJE
Središnje povjerenstvo za završne i diplomske ispite
Povjerenstvo za završne i diplomske ispite studija zrakoplovstva/zrakoplovnog inženjerstva

Sveučilište u Zagrebu Fakultet strojarstva i brodogradnje	
Datum	Prilog
Klasa: **602 - 04 / 24 - 06 / 1**	
Ur.broj: **15 - 24 -**	

DIPLOMSKI ZADATAK

Student: **Magdalena Vuković** JMBAG: 0119044507

Naslov rada na hrvatskom jeziku: **Unaprjeđenje uzdužnog aerodinamičkog modela aviona opće avijacije s modelom povijanja struje i utjecaja tla**

Naslov rada na engleskom jeziku: **Improvement of the longitudinal aerodynamic model for general aviation aircraft with downwash and ground effect models**

Opis zadatka:

The Centre for Aviation at the ZHAW School of Engineering has been developing a flight simulation model of the Piper PA-28-161 Warrior III. As part of various student theses, two flight test campaigns have been conducted to measure the aircraft's flight characteristics during different manoeuvres. The collected data has been used to develop and refine many aspects of the simulation model. Preceding theses used regression and the output-error method to find parameters of the aerodynamic model.

The main goal of this thesis is to improve the existing longitudinal aerodynamic model with separate aerodynamic influences from wing-body, tail, flaps, kinetic pressure loss. Focus of the thesis is on implementation of downwash and ground effects models. These elements, for a conventional configuration as one being analyzed, can be estimated according to the handbook methods.

Following tasks should be performed within the Thesis:

- Implementation of downwash model,
- Implementation of ground effect model,
- Implementation of additional improvements of the existing model: implementation of kinetic pressure loss model, separation of wing-body and tail parameters, estimation of single-slotted flaps model for lift, pitching moment and drag,
- Comparisons of improved and existing aerodynamic model, together with comparison of separate effects with other available results

Thesis should list used bibliography, and any assistance received.

Zadatak zadan:	Datum predaje rada:	Predviđeni datumi obrane:
26. rujna 2024.	28. studeni 2024.	5., 6. i 9. prosinca 2024.

Zadatak zadao:

Prof. dr.sc. Milan Vrdoljak

Dr. Pierluigi Capone

Predsjednik Povjerenstva:

Prof. dr. sc. Milan Vrdoljak

Table of contents

List of figures

List of tables

List of symbols

Symbol	Unit	Description
A	-	aspect ratio
b	m	span
b_{eff}	m	effective span
c	m	aerodynamic chord
$\bar{c}$	m	mean aerodynamic chord
c_t	m	chord of single-slotted flap
Δc_t	m	distance from shroud trailing edge to flap nose measured along flap datum
C_D	-	drag coefficient
C_{Di}	-	induced drag coefficient
C_{D_0}	-	zero lift drag coefficient
c_{d0}	-	airfoil zero lift drag coefficient
$\Delta C_{D_{GE}}$	-	drag coefficient increment in ground effect
C_l	-	rolling moment coefficient
C_L	-	lift coefficient
C_{Lmaxw}	-	maximum lift coefficient of the wing
C_{L_α}	-	lift curve slope
C_{L_0}	-	lift coefficient at zero angle of attack
C_L^*	-	maximum lift coefficient for linear lift curve
ΔC_{Lf}	-	lift coefficient increment due to deployed flaps
$\Delta C_{L_{ht_{GE}}}$	-	horizontal tail lift coefficient increment in ground effect
C_m	-	pitching moment coefficient
ΔC_{m0F}	-	free air pitching moment coefficient increment at zero angle of attack
$\Delta C_{m_{GE}}$	-	pitching moment coefficient increment in ground effect
C_n	-	yawing moment coefficient
C_T	-	thrust coefficient
C_Y	-	side force coefficient
h_{ht}	m	height of horizontal tail aerodynamic centre above the ground
h_w	m	height of wing aerodynamic centre above the ground
i_w	rad	wing incidence angle
K_δ	-	factor for calculating the effective air fold chord with high lift devices deployed
k_1, k_2	-	empirical factors used for calculating effective wingspan
l_t	m	tail lever arm
L	*N*	lift force

$\dot{m}$	$\frac{kg}{s}$	mass flow rate of air inside a cylinder
N	-	empirical factor for calculating ground effect
p	-	factor used to define shape of the non-linear part of the lift curve
q	rad/s	pitch rate
q^*	-	non-dimensional pitch rate
S	m^2	gross planform area of wing
T	N	thrust force
V	m/s	airspeed
$\overline{V}_H$	-	horizontal tail volume
w	m/s	downwash
α	rad	angle of attack
α^*	rad	angle of attach at which maximum lift coefficient for linear lift curve is achieved
α_0	rad	zero lift angle of attack
α_{0w}	rad	wing zero lift angle of attack
β	-	empirical factor for calculating ground effect
γ	-	empirical factor for calculating ground effect
δ	rad	deflection, control surfaces
ε	rad	downwash angle
ε_0	rad	downwash angle at zero angle of attack
$\Delta\varepsilon$	rad	downwash angle increment
ζ	-	wake half-width, in reference to the chord length
ζ'	-	vertical distance from wake centre line, in reference to the chord length
η	Pa	loss in dynamic pressure at wake centre
η'	Pa	loss in dynamic pressure
η_p	Pa	dynamic pressure at a given point
θ	rad	pitch angle
λ	-	taper ratio
ξ	-	distance behind the trailing edge, in reference to the chord length
σ	-	empirical factor for calculating ground effect
τ	-	empirical factor for calculating ground effect
ϕ	-	empirical factor for calculating ground effect
ϕ_0	-	part span factor for outboard limit of trailing edge
ϕ_i	-	part span factor for inboard limit of trailing edge

Indexes

e	elevator
e,TR	elevator trim tab
f	flaps
F	free air
GE	ground effect
ht	horizontal tail
$latdir$	lateral direction
lon	longitudinal
$stall$	stall
wb	wing-body

SUMMARY

The Centre for Aviation at the ZHAW School of Engineering has been developing a flight simulation model of the Piper PA-28-161 Warrior III for research purposes, based on data from two flight test campaigns conducted by students. Previous work focused on estimating aerodynamic parameters and improving the control force model but faced limitations in the flap model, downwash effects, and ground effect representation.

This thesis addresses these issues by introducing a new single-slotted flap model using ESDU methods, a new downwash model accounting for wing wake effects on the tailplane, and an improved ground effect model for lift and pitching moment near the ground. These updates enhance the simulation's accuracy, particularly at low speeds with deployed flaps.

Despite limited flight test data for some configurations, the updated model demonstrates better predictions of lift and pitching moment compared to the previous version. These improvements provide a more realistic simulation of the PA-28's performance and create a foundation for future refinements.

Key words:

Piper PA-28-161 Warrior III, flight simulation, aerodynamic model, downwash, ground effect, flaps,, longitudinal aerodynamics, lift, drag and pitching moment

coefficients

SAŽETAK

Centar za zrakoplovstvo ZHAW škole strojarstva razvija model simulacije leta Piper PA-28-161 Warrior-a III u istraživačke svrhe, temeljen na podacima prikupljenim tijekom dviju studentskih letnih kampanja. Prethodni radovi bavili su se procjenom aerodinamičkih parametara i poboljšanjem modela upravljačkih sila, no ostala su ograničenja u modelima zakrilaca, efekta povijanja struje i efekta tla.

Ovaj rad fokusira se na ta ograničenja uvođenjem novog modela za zakrilca s jednim prorezom koristeći ESDU metode, novog modela povijanja struje koji uključuje izračune gradijenta povijanja struje, kuta povijanja struje i gubitka dinamičkog tlaka te poboljšanog modela efekta tla za bolje prikazivanje promjena uzgona i momenta propinjanja tijekom polijetanja i slijetanja.

Unatoč ograničenim podacima za spuštene zakrilce i efekt tla, ažurirani model pokazuje bolju točnost u simulaciji uzdužnog aerodinamičkog ponašanja, posebno pri malim brzinama. Poboljšanja omogućuju realističniju simulaciju performansi PA-28 i pružaju temelj za daljnja istraživanja.

Ključne riječi: Piper PA-28-161 Warrior III, simulacija leta, aerodinamički model, efekt povijanja struje, efekt tla, model zakrilaca, uzdužna aerodinamika, koeficijenti uzgona i momenta propinjanja

PROŠIRENI SAŽETAK

UVOD U PROBLEMATIKU I CILJ RADA

Razvoj modela simulacije leta predstavlja važan doprinos istraživanjima u području zrakoplovstva i obrazovanju budućih pilota. Model leta za zrakoplov Piper PA-28-161 Warrior III, koji je dio istraživačkog rada Centra za zrakoplovstvo ZHAW, temelji se na podacima iz leta prikupljenim tijekom dviju studentskih kampanja. Prethodni radovi omogućili su stvaranje osnovnog aerodinamičkog modela zrakoplova, ali istaknuli su i značajna ograničenja, osobito u modelu zakrilaca, nedostatku modela povijanja struje (eng. *downwash*) i modelu efekta tla. Ta su ograničenja rezultirala manjkom preciznosti pri simulaciji letova s niskim brzinama i velikim napadnim kutovima, posebno u konfiguracijama sa zakrilcima.

Cilj ovog rada je unaprijediti postojeći model uzdužne aerodinamike zrakoplova PA-28 kroz integraciju novih modela zakrilaca, povijanja struje i efekta tla, koristeći klasičnu literaturu te metode iz ESDU i NACA dokumenata. Očekuje se da će unaprijeđeni model omogućiti realističniju simulaciju leta, osobito u fazama polijetanja i slijetanja.

Slika I Simulator leta Centra za zrakoplovstvo ZHAW

DOSADAŠNJA ISTRAŽIVANJA I OGRANIČENJA POSTOJEĆEG MODELA

Postojeći linearni modeli uzdužne i bočne aerodinamike zrakoplova Piper PA-28 razvijeni su u okviru Pedrazzinijeva rada s ciljem preciznijeg opisivanja statičkog i dinamičkog ponašanja zrakoplova. Pedrazzini je koristio podatke prikupljene tijekom dviju kampanja letnih testova. Tijekom prve kampanje prikupljeni su podaci o napadnom kutu i dinamičkom tlaku, dok je druga kampanja zahtijevala obradu video snimki zbog nedostatka mjernih uređaja poput air data boom-a. Njegov rad omogućio je proširenje modela kako bi uključio pojavu sloma uzgona, model zakrilaca i efekta tla, čime je omogućena detaljnija analiza aerodinamičkog ponašanja zrakoplova u različitim uvjetima leta. Međutim, iako su rezultati donijeli značajne doprinose, nekoliko ključnih ograničenja ostalo je neriješeno, posebno u pogledu modeliranja zakrilaca.

Jedno od glavnih ograničenja postojećeg uzdužnog modela je manjak točnosti u modeliranju zakrilaca. Pedrazzinijev model koristio je pojednostavljenu aproksimaciju običnih zakrilaca, koja nije uzela u obzir karakteristike zakrilaca s jednim prorezom kakve ima zrakoplov PA-28. Nedostatak podataka prikupljenih za različite postavke zakrilaca dodatno je ograničio preciznost modela. Tijekom prve kampanje testova leta, većina manevara izvedena je s potpuno uvučenim zakrilcima, dok su konfiguracije sa zakrilcima otklonjenim na 0°, 25° i 40° korištene samo pri slijetanju. Druga kampanja uključivala je manevre s izvučenim zakrilcima, ali zbog nedostatka mjerenja ključnih parametara poput napadnog kuta, ti podaci nisu bili uporabivi.

Model povijanja struje, koji utječe na interakciju između krila i horizontalnog stabilizatora, nije bio integriran u prethodni model. To je rezultiralo manjkom preciznosti u procjeni uzgona horizontalnog stabilatora i momenta propinjanja, osobito pri velikim napadnim kutovima.

Efekt tla, ključan za faze polijetanja i slijetanja, također je bio ograničeno modeliran. Pedrazzini je koristio jednostavnu aproksimaciju prema Jategaonkaru, koja predviđa promjene u uzgonu i momentu propinjanja u blizini tla. Međutim, parametri potrebni za proračun ovog modela bili su slobodno procjenjeni radi ograničenih podataka prikupljenih tijekom testova polijetanja i slijetanja, koji nisu omogućili daljnje prilagodbe modela.

UNAPREĐENJE MODELA UZDUŽNE AERODINAMIKE

Unapređenje modela uzdužne aerodinamike zrakoplova PA-28 započelo je detaljnom analizom postojećeg modela, uključujući separaciju varijabli. Ovaj pristup omogućio je preciznije razdvajanje utjecaja krila i trupa od utjecaja horizontalnog stabilizatora na ukupnu aerodinamiku zrakoplova. Separacija varijabli pružila je temelje za razumijevanje pojedinačnih

doprinosa kombinacije krilo-trup i repa te njihov utjecaj na aerodinamičke sile i momente zrakoplova, što je ključno za daljnje modeliranje i optimizaciju.

Modeliranje zakrilaca

Razvijen je novi model zakrilaca, prilagođen za zakrilca s jednim prorezom. Korištene su metode iz ESDU dokumenata, uključujući ESDU 96003 62[12], koji omogućuje preciznu procjenu promjene koeficijenta uzgona zbog zakrilaca. Uzgon je modeliran u dvije faze: linearni dio uzgona do napadnog kuta pri kojem započinje razdvajanje strujanja i nelinearni dio koji se proteže do koeficijenta maksmalnog uzgona. Također, povećanje otpora uzrokovano zakrilcima modelirano je pomoću metode opisane u ESDU 08013 [20], s naglaskom na odvajanje doprinosa otpora profila i induciranog otpora. Promjene momenta propinjanja uzrokovane zakrilcima, uključujuči pomicanje aerodinamičkog centra, izračunate su koristeći ESDU 03017 [26]. Validacija rezultata provedena je pomoću softvera XFLR5, koji je pružio okvir za usporedbu s teorijskim izračunima iz ESDU dokumenata.

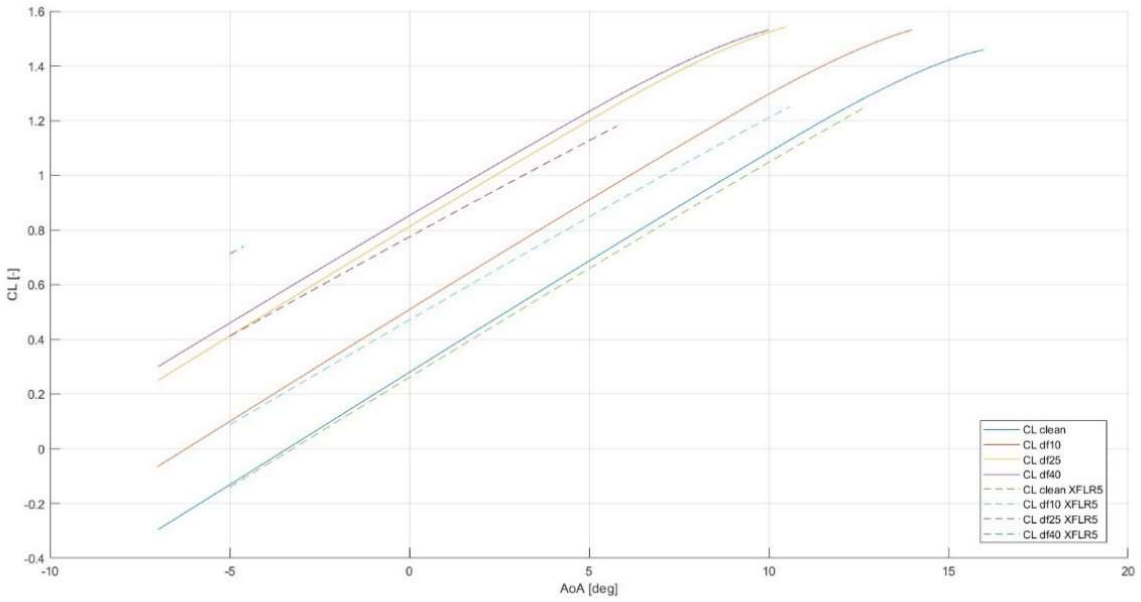

Slika II Usporedba koeficijenta uzgona krila - ESDU metoda i XFLR5

Model povijanja struje

Povijanje struje predstavlja ključnu komponentu aerodinamičkog modeliranja, posebno u analizi interakcije između krila i horizontalnog stabilizatora. Ovaj fenomen proizlazi iz uzgona generiranog na krilu, koji stvara sustav vrtloga u struji iza krila, uzrokujući da se struja zraka u

tragu iza krila spušta prema dolje. Ovo strujanje definirano je kutom povijanja ε, koji mijenja efektivni napadni kut horizontalnog stabilizatora.

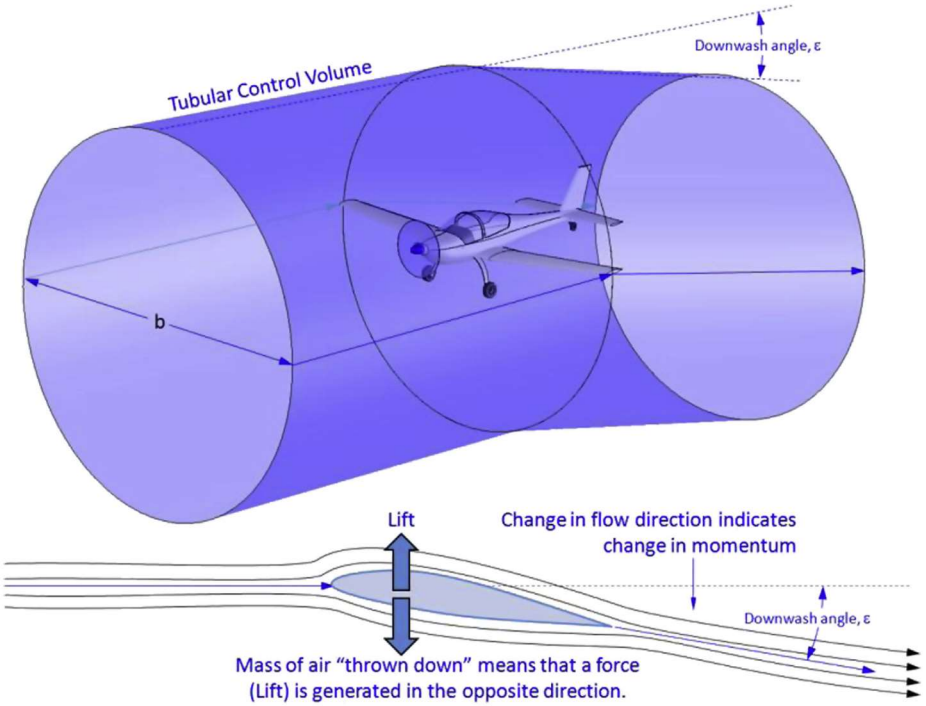

Slika III Povijanje struje [30]

Gudmundssonova metoda pruža jednostavan i direktan pristup za početnu procjenu gradijenta povijanja struje. Metoda pretpostavlja idealizirane uvjete za krilo i pruža korisne aproksimacije za početno modeliranje povijanja. Gradijent povijanja struje, koji opisuje promjenu kuta povijanja s promjenom napadnog kuta, izračunava se kao [30]:

$$\frac{d\varepsilon}{d\alpha} = \frac{2}{\pi A}\frac{d}{d\alpha}\left(C_{L_0} + C_{L_\alpha}\alpha\right) = \frac{2C_{L_\alpha}}{\pi A} \qquad \textbf{(I)}$$

Za preciznije procjene kuta povijanja struje ε, korišten je NACA Report No. 648 64 [35], koji uključuje grafičke prikaze i empirijske podatke o povijanju struje za različite konfiguracije krila i zakrilaca. Ovaj dokument omogućuje:

1. Procjenu kuta povijanja za krila s različitim postavkama zakrilaca, uključujući otklone od 0°, 25° i 40°.
2. Analizu gubitka dinamičkog tlaka na horizontalnom stabilizatoru uzrokovanog vrtložnim tragom iza krila.

Izvještaj koristi detaljne dijagrame i grafove za određivanje kuta povijanja struje, uzimajući u obzir doprinos zakrilaca. Gubitak dinamičkog tlaka računa se ovisno o položaju stabilizatora unutar vrtložnog traga. Ovaj gubitak izravno utječe na uzgon i moment koji generira stabilizator, čineći ga ključnim parametrom u modeliranju aerodinamičkog ponašanja zrakoplova.

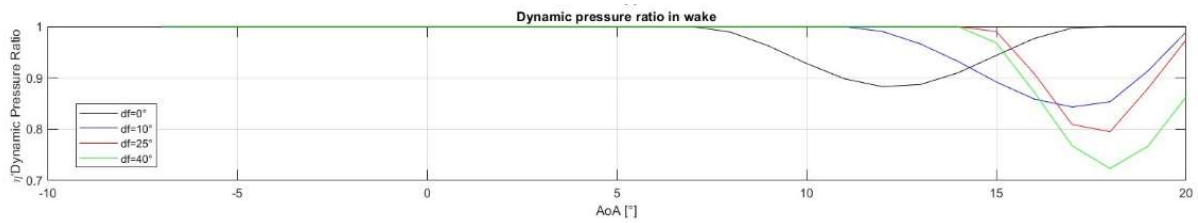

Slika IV Gubitak dinamičkog tlaka u tragu

Model efekta tla

Efekt tla značajno mijenja aerodinamičke karakteristike zrakoplova tijekom faza polijetanja i slijetanja. Blizina tla povećava uzgon i utječe na aerodinamičke momente. U ovom radu model efekta tla temelji se na teorijskim osnovama i prilagodbi postojećih jednadžbi za opisivanje aerodinamičkih koeficijenata u blizini tla [36].

Uzgon se povećava zbog stvaranja efekta "zračnog jastuka" između krila i tla. Koeficijent uzgona u blizini tla izražen je kao suma uzgona u slobodnom zraku i povećanja uzgona zbog efekta tla. Ovo povećanje ovisi o geometriji krila, visini krila iznad tla te drugim geometrijskim parametrima.

Efekt tla također smanjuje kut povijanja struje na horizontalnom stabilizatoru, što dovodi do promjena u momentu propinjanja. Smanjenje kuta povijanja struje izraženo je kroz dodatak $\Delta\varepsilon$, koji ovisi o visini horizontalnog stabilizatora iznad tla i interakciji između krila i stabilizatora. Moment je modeliran uzimajući u obzir udaljenost poluge između aerodinamičkog centra krila i repne površine te iznos promjene sile uzgona koja djeluje na horizontalni stabilizator.

Promjena induciranog otpora jedan je od ključnih utjecaja efekta tla. Koeficijent otpora u blizini tla računa se kao suma koeficijenta otpora u slobodnom zraku i promjene induciranog otpora. Ovaj model zasniva se na promjeni koeficijenta uzgona zbog blizine tla. Proračuni za otpor su isključeni iz konačnog modela radi strukture osnovnog modela.

IMPLEMENTACIJA MODELA

Postojeći MATLAB i Simulink modeli za simulaciju zrakoplova PA-28 prilagođeni su integracijom novih aerodinamičkih modela. Skripta *iniac.m*, koja definira ključne parametre zrakoplova, ažurirana je kako bi uključila nove koeficijente uzgona, otpora i momenta propinjanja za zakrilca, izračunate prema ESDU metodama. Parametri su ručno prilagođeni radi usklađivanja s ostatkom simulacije.

U Simulink modelu *model_aero.slx*, implementirani su blokovi za povijanje struje, uključujući napadni kut stabilizatora i dinamički tlak, kako bi se preciznije modelirali utjecaji glavnog krila na horizontalni stabilizator. Parametri za gradijent povijanja struje, dodatak kutu povijanja struje radi zakrilaca i parametri za gubitak dinamičkog tlaka, izračunati u prethodnim poglavljima rada, također su definirani u skripti *iniac.m*.

Novi model efekta tla integriran je zamjenom starih blokova s MATLAB funkcijskim blokovima. Ovi blokovi izračunavaju promjene u uzgonu i momentu propinjanja zbog blizine tla, koristeći aerodinamičke podatke iz leta u slobodnoj struji zraka.

REZULTATI

Usporedba novog i starog modela PA-28 pokazala je značajan utjecaj uvedenih promjena na aerodinamičke performanse zrakoplova. Poboljšanje modela zakrilaca jasno je vidljivo u dijagramu uzgona, gdje su razlike najočitije pri većim napadnim kutevima. Novi model ukazuje na značajno povećanje koeficijenta uzgona kod otklona zakrilaca od 10° i 25°, dok je povećanje kod 40° manje izraženo, u skladu s teorijskim očekivanjima. U simulacijama momenta propinjanja utjecaj povijanja struje postao je vidljiv, osobito kod većih otklona zakrilaca, gdje interakcija između glavnog krila i repa značajno mijenja ponašanje zrakoplova. Novi model također točnije bilježi naglo smanjenje momenta kod sloma uzgona, što stariji model nije adekvatno prikazivao. Kod otpora, novi model preciznije simulira dodatni otpor uzrokovan zakrilcima, osobito pri 25° otklona, gdje je razlika najizraženija pri manjim napadnim kutovima zbog otpora oblika profila sa zakrilcima.

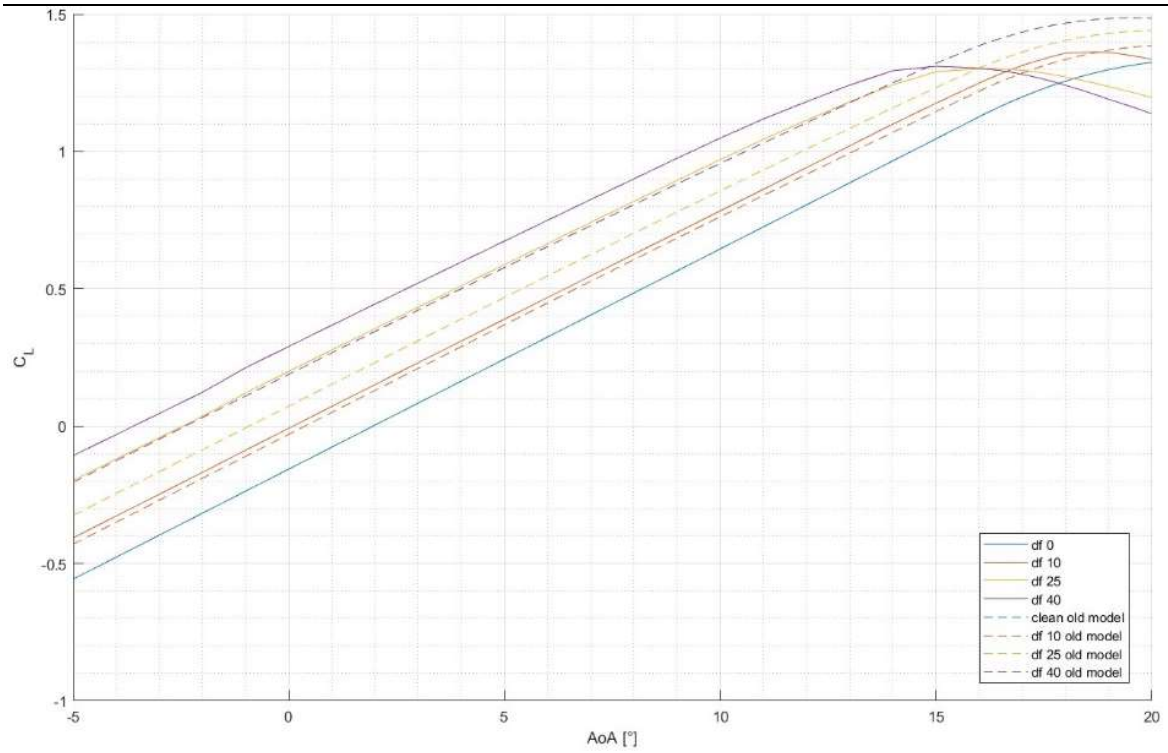

Slika V Usporedba koeficijenta uzgona zrakoplova - novi i stari model

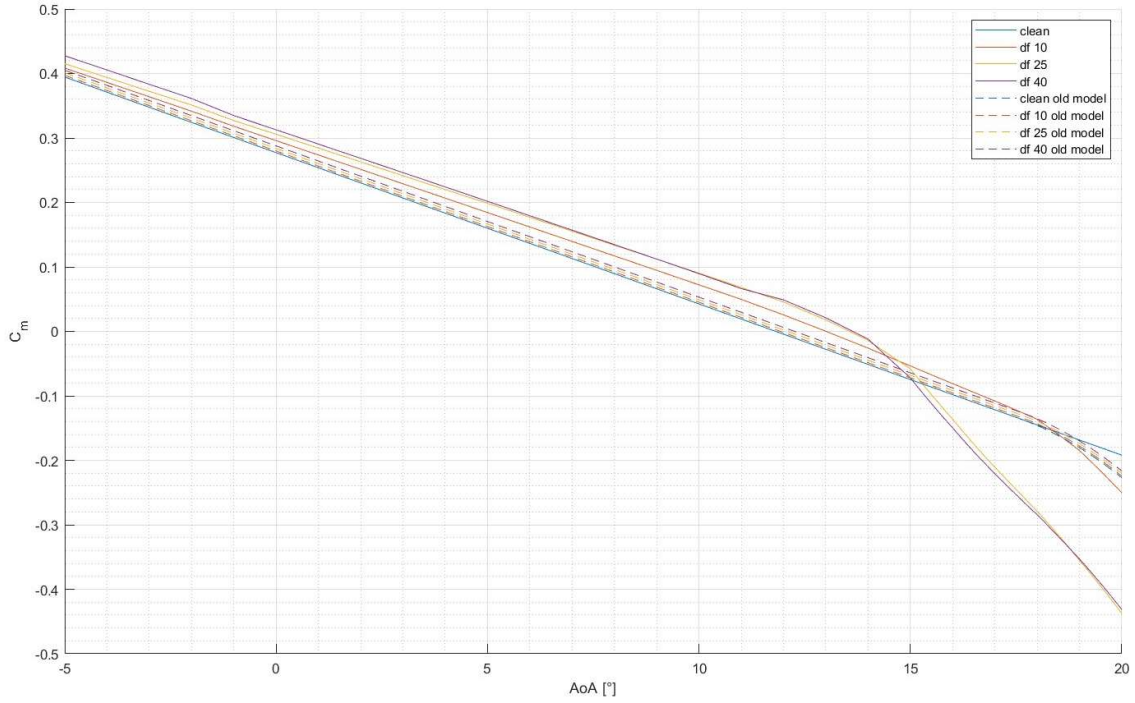

Slika VI Usporedba koeficijenta momenta propinjanja zrakoplova - novi i stari model

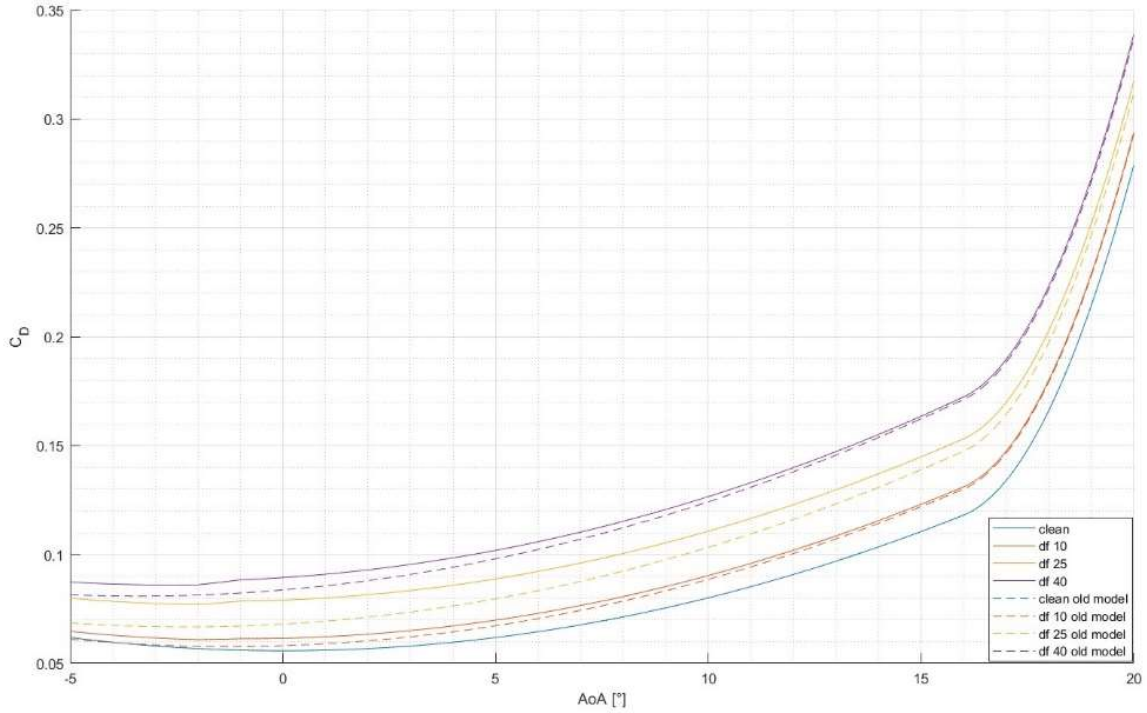

Slika VII Usporedba koeficijenta otpora zrakoplova - novi i stari model

Utjecaj povijanja struje i korekcije momenta propinjanja zbog zakrilaca najbolje se vidi u rezultatima trim testa izvedenog na simulatoru. Novi model u usporedbi sa starim, pokazuje lagano povećanje kuta propinjanja za istu konfiguraciju zakrilaca i napadni kut (*Tablica I*), što je rezultat smanjenog uzgona repne površine zbog povijanja struje.

Tablica I Usporedba rezultata trim testa za stari i novi model

δ_f [°]	θ [°]		α [°]	
	S_O	S_N	S_O	S_N
0	6.5	7.1	6.6	6.7
10	5.6	6.6	5.0	5.2
25	4.1	4.7	4.0	4.1
40	3.2	3.5	3.3	3.3

Promjene u modelu efekta tla najjasnije su vidljive u scenarijima slijetanja. Za iste parametre brzine leta i okretaja motora, novi model pokazuje veću usklađenost s podacima iz testova leta.

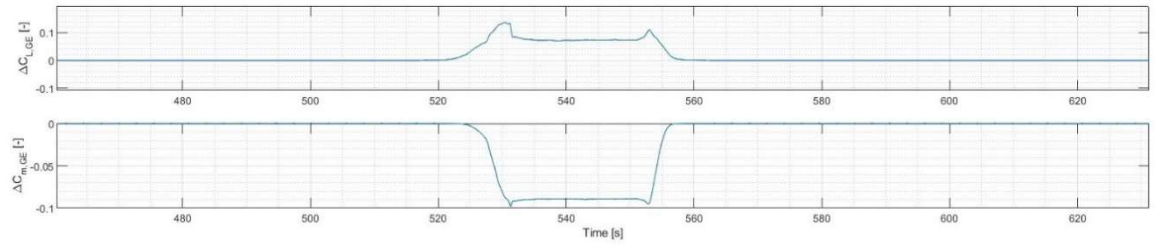

Slika VIII Promjena koeficijenta uzgona i momenta propinjanja u efektu tla - stari model, konfiguracija s uvučenim zakrilcima

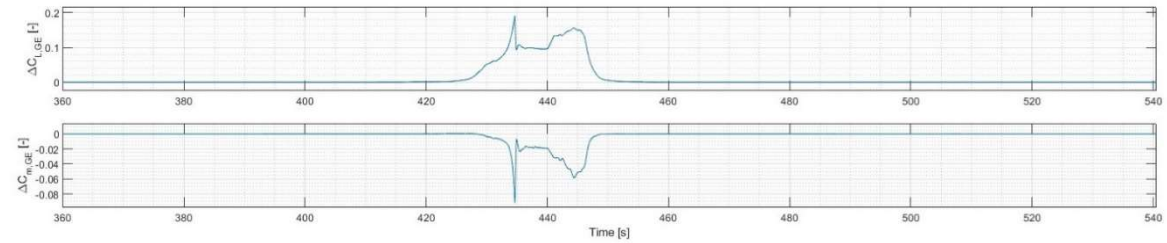

Slika IX Promjena koeficijenta uzgona i momenta propinjanja u efektu tla - novi model, konfiguracija s uvučenim zakrilcima

Kod konfiguracije bez zakrilaca, razlike između starog i novog modela pokazuju značajan porast uzgona i smanjenje momenta propinjanja zbog smanjenog povijanja struje na repu. Kod konfiguracija sa zakrilcima, novi model prati isti trend.

Važno je naglasiti da prjelazna dinamika nije razmatrana u ovom radu.

ZAKLJUČAK

Ovim radom simulacijski model PA-28 je unaprijeđena su tri ključna područja: model zakrilaca, model povijanja struje i model efekta tla. Novi model zakrilaca, razvijen prema ESDU metodama, preciznije predviđa koeficijente uzgona, otpora i momenta propinjanja za postavke zakrilaca od 10°, 25° i 40°. Integracija modela povijanja struje poboljšala je simulaciju interakcija između krila i repa, uključujući promjene uzgona i momenta uzrokovane kutom povijanja i gubitkom dinamičkog tlaka. Ažurirani model efekta tla pružio je realističniju procjenu aerodinamičkih promjena tijekom polijetanja i slijetanja, unatoč ograničenim podacima iz letnih testova.

Ipak, određene limitacije ostaju. Nedostatak podataka o ponašanju zrakoplova pri gubitku uzgona ograničio je preciznost modela u tim uvjetima. Učinak povijanja struje na stabilnost

tijekom dinamičkih manevara nije istražen, dok su rezultati efekta tla mogli biti precizniji s dodatnim letnim testovima. Male pogreške u otklonu elevatora i momenta propinjanja ukazuju na potrebu za finijim podešavanjem parametara simulacije. Buduća istraživanja trebala bi se fokusirati na ova područja kako bi se model dodatno poboljšao i omogućio precizniju simulaciju.

1. INTRODUCTION

Flight simulation is a powerful tool primarily used for research, development, and pilot training. Within the Centre for Aviation (Zentrum für Aviatik, ZAV) at the ZHAW School of Engineering, students and researchers collaborate to develop aircraft simulation models for research and interactive pilot-in-the-loop simulations. One of the models being developed is the flight simulation model for the Piper PA-28-161 Warrior III.

Piper PA-28-161 Warrior III is a single engine piston aircraft, widely used for pilot training since its introduction in 1994. [1].

1.1. Background of the PA-28 project

Work on the PA-28 simulator model began with two flight test campaigns. Both campaigns were conducted by students and performed using the same aircraft. During these campaigns, flight data was collected using an air data boom and video recording of the flight instruments [2].

During the first flight test campaign, conducted by Ferrari and Spillmann in 2019., aerodynamic parameters such as angle of attack and dynamic air pressure were collected. Following the first campaign, as part of projects for the Master theses, the parameters for aerodynamic coefficients were estimated and the flight path was reconstruction was done [3][4].

The focus of the second campaign, conducted by Pedrazzini and Püntener in 2021, was the instrumentation of pilot control forces and video recordings of the flight instruments. Pedrazzini continued working on the PA-28 model in his master's thesis, focusing on improving both the aerodynamic and control force models using the output-error method for parameter estimation[2].

1.2. Current PA-28-161 Warrior III model

The original PA-28 flight simulator model was built in MATLAB Simulink and is intended for educational and research purposes. It is based on a six-degrees-of-freedom (6DOF) model in which the forces acting on the aircraft are a function of the current aircraft state and control inputs.

Spillmann developed a script for calculating the aircrafts centre of gravity and moment of inertia, based on user input for weight and balance[5].

Initially, the aerodynamic coefficients in the stability axes were estimated using regression to fit the model to the data collected during the first flight test campaign[3][4]. Limitations of this model most relevant to this thesis were simplified flap and control surfaces model and unrealistic performance at low speeds, requiring higher-than-realistic approach speeds leading to lower lift and increased drag, especially at high angles of attack or with extended flaps [2].

Pedrazzini worked on improving the aerodynamic model as well as the control force model.

The new model used the output-error method to refine aerodynamic and stability coefficients, achieving a closer match to flight test data. This method compared model outputs to actual flight test data, adjusting parameters iteratively to reduce differences between the simulated values and real flight data. The optimized model could replicate the frequency and amplitude of the aircraft's natural oscillatory modes, bringing the model closer to the real aircraft's response [2].

The control force model was updated to reflect more realistic feedback from control inputs, validated against test data from the PA-28. Control input response improved, though minor differences remained in trimming, likely due to small errors in the flight data [2].

The lift and pitching contributions of the stabilator and the trim tab were optimized as well.

As the flight test data had few records of extended flap configurations, flap performance was estimated using literature values and manual adjustments to match flight data, but did not account for PA-28s single slotted flap and instead used a simpler model for plain flaps [2].

One significant limitation of the new model was the lack of an integrated downwash effect. Downwash, which is the downward airflow induced by the wing, typically impacts the horizontal stabilizer and influences the tail's lift and pitching moment. Due to the missing downwash model and simplified flaps model, the tail lift and pitching moment contributions were not very accurate especially in low-speed conditions where downwash effects are more pronounced[2].

Additionally, ground effect was not a focus in either of the flight test campaigns, resulting in only limited data on take-offs and landings. Because of that, in his thesis, Pedrazzini used a very basic ground effect model and manually estimated parameters related to ground effect [2].

1.3. Objectives of the thesis

The goal of this thesis is to make the PA-28 flight simulation model more accurate and realistic by improving the existing longitudinal aerodynamic model and adding the downwash and ground effect models.

Based on Pedrazzini's previous work [2], the wing-body and tail dynamics will be separated, and a more precise single-slotted flap model will be implemented. This includes re-evaluating lift, drag and pitching moment for the flaps model and using detailed methods from ESDU and NACA to make these calculations more accurate. By doing this, the model will better reflect how the flaps affect lift, drag and pitching moment in real flight conditions, especially during take-off and landing.

As the downwash model is missing in earlier versions of the PA-28 flight simulation model, this thesis will focus on developing and integrating the downwash model, by calculating the downwash gradient and estimating downwash angle for both clean configuration and flaps deployed configuration.

Additionally, kinetic pressure loss at the tail plane will be estimated as it is directly connected to downwash and air stream displacement and simulates tail dynamics more consistently.

Using the limited data that is available, a more detailed ground effect model will be developed and implemented.

The final goal is to incorporate these improvements into the existing MATLAB Simulink model of the PA-28. This will involve updating the aerodynamic parameters, adding the downwash and refined flap models, and integrating a ground effect model. The improved model will be compared with the original version to assess improvements in accuracy, particularly in lift and pitching moment.

2. THEORIES AND REFERENCE MATERIALS FOR LONGITUDINAL AERODYNAMICS

In this thesis, a mix of fundamental and specialized resources will be used to improve the PA-28 simulation model. Key textbooks on aerodynamics will provide the theories for modelling downwash and ground effect. Alongside these, specific research documents, such as ESDU datasheets and NACA technical reports, will offer reliable methods and precise calculations for tackling the more complex flaps model calculations. These aerospace and engineering resources will be crucial for refining aerodynamic parameters and enhancing the model.

2.1. ESDU and NACA documents

ESDU and NACA documents are valuable resources that provide strong theoretical methods backed by extensive experimental data and tested models. They combine aerodynamic principles with practical, real-world data to solve complex engineering problems.

2.1.1. ESDU datasheets

ESDU (*Engineering Sciences Data Unit*) is widely used by international aerospace companies and other engineering industries. ESDU is an engineering knowledge repository that provides validated design methods, data and software tools covering a wide range of engineering disciplines. Leading experts from industry, academia and government organizations from around the world collaborate to monitor and validate the work of ESDU engineers [6].

2.1.2. NACA Technical Publications

The U.S. government formed the NACA (*the National Advisory Committee for Aeronautics*) in 1915 to accelerate aeronautical research. After more than 40 years of groundbreaking research into aeronautics, the NACA was transformed into NASA (*National Aeronautics and Space Administration*) in 1958 and given the added task of spaceflight [7].

NASA Technical Report Server (NTRS) is a bibliographic database of selected reports intended to make research more available [8].

The NACA reports are still widely used by researchers and students today, offering valuable insights and data that support ongoing work in aeronautics.

3. CURRENT AERODYNAMIC MODEL

In his master's thesis [2], Pedrazzini worked on improving the linear longitudinal and lateral-directional aerodynamic model of the PA-28 to capture both static and dynamic aircraft behaviour.

To prepare data for the model, Pedrazzini applied methods to filter, correct errors, and process the information. Using data from the first flight test campaign, he corrected errors in extracted data used in the model to improve accuracy, while data from the second campaign required the processing of video recordings.

Pedrazzini defined a linear longitudinal and lateral-directional aerodynamic model, which he expanded to include the effects of stall, flaps and ground effect.

Equations (3.1)-(3.6) show the main structure of the aerodynamic coefficients [2].

$$C_L = C_{L_{lon}} + C_{L_{latdir}} + C_{L_{\delta_f}} + C_{L_{stall}} + C_{L_{GE}} \quad \textbf{(3.1)}$$

$$C_D = C_{D_{lon}} + C_{D_{latdir}} + C_{D_{\delta_f}} + C_{D_{stall}} \quad \textbf{(3.2)}$$

$$C_m = C_{m_{lon}} + C_{m_{\delta_f}} + C_{D_{stall}} + C_{m_{GE}} \quad \textbf{(3.3)}$$

$$C_Y = C_{Y_{latdir}} \quad \textbf{(3.4)}$$

$$C_l = C_{l_{latdir}} \quad \textbf{(3.5)}$$

$$C_n = C_{n_{latdir}} \quad \textbf{(3.6)}$$

The parameter estimations for the longitudinal aerodynamic model were divided into three parts: longitudinal translation, static trimmed flight and dynamic flight. A specific set of manoeuvres from the first flight test campaign were selected for these estimations [2].

Similarly, Pedrazzini split the lateral-directional aerodynamic model parameter estimations into different parts, using a similar approach as he did for the longitudinal aerodynamic model. This included simulating lateral translation, yaw motion, roll motion, and combined roll and yaw motion. This approach allowed Pedrazzini to thoroughly analyse the aircraft's aerodynamic behaviour across various flight conditions and manoeuvres, creating a more complete aerodynamic model [2].

This thesis will focus exclusively on the longitudinal model, examining individual aspects of longitudinal aerodynamics in detail to improve accuracy and reliability of the model.

3.1. Existing longitudinal aerodynamic model

Pedrazzini estimated the parameters of the longitudinal aerodynamic model using the linear regression and output-error method.

Structure of Pedrazzini's linear longitudinal aerodynamic model (Eq. 3.7-3.10) [2]:

$$C_{L_{lon}} = C_{L_0} + \alpha \cdot C_{L_\alpha} + q^* \cdot C_{L_{q^*}} + C_T \cdot C_{L_{C_T}} + \frac{S_H}{S} C_{L_T} \quad \textbf{(3.7)}$$

$$C_{L_T} = \delta_e \cdot C_{L_{T,\delta_e}} + \delta_{e,TR} \cdot C_{L_{T,\delta_{e,TR}}} \quad \textbf{(3.8)}$$

$$C_{D_{lon}} = C_{D_0} + \alpha^2 \cdot C_{D_{\alpha^2}} + C_T \cdot C_{D_{C_T}} \quad \textbf{(3.9)}$$

$$C_{m_{lon}} = C_{m_0} + \alpha \cdot C_{m_\alpha} + q^* \cdot C_{m_{q^*}} + C_T \cdot C_{m_{C_T}} - \frac{l_t S_H}{\bar{c} S} C_{L_T} \quad \textbf{(3.10)}$$

The tail lift C_{L_T} model includes the stabilator deflection δ_e, which is crucial as the entire horizontal tail pivots around the hinge to act as the elevator, sometimes described in literature as a "flying tail". Due to the significant size of the stabilator trim tab, the aerodynamic effect of this surface was modelled as well, using the term $C_{L_{T,\delta_{e,TR}}}$ [2].

The pitching moment contribution is expressed by the tail lift force and the appropriate lever arm. This was done to reduce the number of parameters that had to be estimated and to increase fidelity at small angles of attack, as it represents the real behaviour of a force and its lever arm generating a pitching moment [2].

Pedrazzini introduced the thrust coefficient C_T and the corresponding coefficients $C_{L_{C_T}}, C_{D_{C_T}}$ and $C_{m_{C_T}}$ in an effort to model the effect of down- and sideslip propwash. However, the model has many limitations and is not considered reliable [2].

3.2. Existing flaps and ground effect approximations

3.2.1. Flaps

The first flight test campaign provided data for aerodynamic modelling, but it did not include systematic tests for different flap settings. All primary manoeuvres were performed with the flaps fully retracted, except for landings, where flap settings of 0°, 25°, and 40° were used [2]. In the second flight test campaign, some manoeuvres were flown with flap deflection, but the aircraft was missing an air data boom. This meant key parameters like angle of attack were not recorded, rendering this data unusable [2].

Therefore, Pedrazzini estimated the aerodynamic effects of flap deployment using theoretical methods described in ESDU documents. It is important to point out that Pedrazzini used

documents which described lift curve of wings with full-span plain flaps deployed at low speeds [2].

The effect of flap deflection on pitching moment was estimated manually, assumed to be linear. Coefficient $C_{m_{\delta_f}}$ was added to approximate the flight conditions of the test aircraft [2].

3.2.2. Ground effect

Ground effect was not a primary focus of either of the flight test campaigns, so there was only limited data available from take-offs and landings. Because of this data shortage, Pedrazzini manually estimated the parameters for ground effect.

A very simple model by Jategaonkar [9], shown in equations 3.11-3.14 was chosen as it captures the effects ground effect has on increase in wing lift curve slope and increase in tail lift curve slope [2].

$$C_{L_{GE}} = \sigma \cdot \alpha \cdot C_{L_{\alpha,GE}} \quad \textbf{(3.11)}$$

$$C_{m_{GE}} = \sigma_{stab} \cdot C_{m_{GE}} \quad \textbf{(3.12)}$$

$$\sigma = 1 - \tanh\left(a\frac{h}{b}\right) \quad \textbf{(3.13)}$$

$$\sigma_{stab} = 1 - \tanh\left(a_{ht}\frac{h_{ht}}{b_{ht}}\right) \quad \textbf{(3.14)}$$

4. MODELING OF WING-BODY, TAIL, AND FLAP AERODYNAMIC EFFECTS

4.1. Wing-body and tail aerodynamic influence separation

Pedrazzini estimated the parameters for the longitudinal model using linear regression, with all force and moment coefficients referenced directly to the aircraft [2].

To improve the model's precision, variable separation is applied, breaking down the coefficients to show the individual aerodynamic influence of the wing-body and tail. This method provides a clearer understanding of how each component influences the aerodynamic forces and moments acting on the aircraft, allowing the model to more accurately reflect the aircraft's real aerodynamic behaviour across different flight conditions.

Structure of Pedrazzini's linear longitudinal lift coefficient and highlighted tail lift coefficient [2] is shown in equations 4.1 and 4.2.

$$C_{L_{lon}} = C_{L_0} + C_{L_\alpha}\alpha + q * C_{L_q} + C_T C_{L_{CT}} + \frac{S_{ht}}{S} C_{L_T} \tag{4.1}$$

$$C_{L_T} = (\delta_e C_{L_{ht,\delta e}} + \delta_{e,TR} C_{L_{ht,\delta_{e,TR}}}) \tag{4.2}$$

After the separation of variables, the coefficient structure becomes (Eq. 4.3-4.5):

$$C_{L_\alpha} = C_{L_{\alpha_{wb}}} + C_{L_{\alpha_{ht}}} \eta_{ht} \frac{S_{ht}}{S} (1 - \frac{\partial \varepsilon}{\partial \alpha}) \tag{4.3}$$

$$C_{L_0} = C_{L_{0_{wb}}} + C_{L_{0_{ht}}} = C_{L_{\alpha_{wb}}} (i_w - \alpha_{0_{wb}}) \tag{4.4}$$

$$C_{L_T} = \eta_{ht} \left(C_{L_{\alpha_{ht}}} (\alpha - \alpha \frac{\partial \varepsilon}{\partial \alpha} + \delta_e - \varepsilon_0) + \delta_{e,TR} C_{L_{ht,\delta_{e,TR}}} \right) \tag{4.5}$$

Variable separation for the longitudinal lift coefficients was conducted by applying a systematic process to isolate the effects of the wing-body and tail, as outlined in the following points.

1. Conditions and constants are defined, including elevator deflection and elevator trim tab deflection. Two angles of attack are also set as key reference points for the analysis.
2. Measured lift coefficients C_L in clean configuration specified for each angle of attack using Pedrazzini's model.
3. Two equations are set up for the two angles of attack to solve for the wing-body lift coefficient $C_{L_{0_{wb}}}$ and the lift curve slope $C_{L_{\alpha_{wb}}}$ by constructing a matrix equation. These equations are arranged in a way where the left-hand sides are equal to each

other. Therefore, by subtracting known parts of the new model from the determined C_L for a given alpha, the coefficient $C_{L_{0_{wb}}}$ and lift curve slope $C_{L_{\alpha_{wb}}}$ can be calculated.

Equation (4.6) highlights how the coefficient values needed for the variable separation are calculated and obtained:

$$C_L = C_{L_{0_{wb}}} + C_{L_{\alpha_{wb}}}\alpha + q^* C_{L_q} + C_T C_{L_{CT}} + \eta_{ht}\frac{S_{ht}}{S}\left[C_{L_{\alpha_{ht}}}\left(\alpha - \alpha\frac{\partial\varepsilon}{\partial\alpha} + \delta_e - \varepsilon_0\right) + \delta_{e,TR}C_{L_{ht,\delta_{e,TR}}}\right] \quad (4.6)$$

- Reliable value from Pedrazzini's model.
- Unreliable value from Pedrazzini's model 62[2] – propeller thrust model improvement was listed as recommendation for further work, but it is out of scope of this thesis.
- Will be calculated in following chapters.

Figure 1 is an example of a visualization of the process.

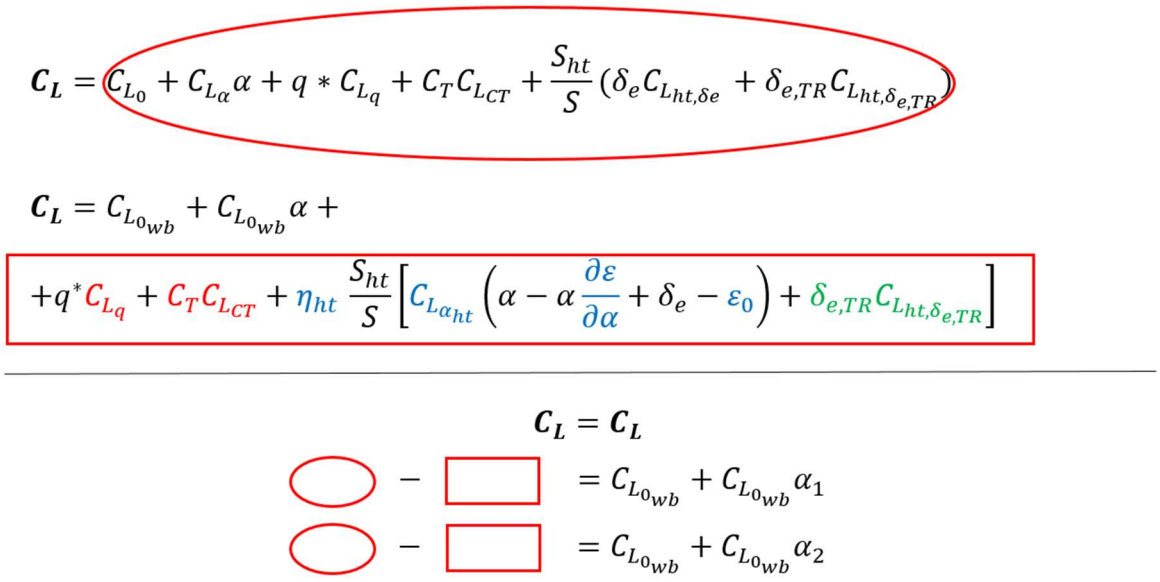

Figure 1 Visualization of the process for variable separation - lift model

Value of $C_{L_{\alpha_{ht}}}$ was corrected for body mounted tailplane according to ESDU 89029 [10]. Calculation of other values that are highlighted in blue in *Figure 1* will be explained in further chapters in this thesis.

Equations (4.7) and (4.8) show the structure of Pedrazzini's linear longitudinal pitching moment coefficient.

$$C_m = C_{m_0} + C_{m_\alpha}\alpha + q * C_{m_q} + C_T C_{L_{CT}} - \frac{l_t S_{ht}}{\bar{c}\, S} C_{L_T} \quad \textbf{(4.7)}$$

$$C_{L_T} = (\delta_e C_{L_{ht,\delta e}} + \delta_{e,TR} C_{L_{ht,\delta_{e,TR}}}) \quad \textbf{(4.8)}$$

After the separation of variables, the coefficient structure is (Eq. 4.9-4.11):

$$C_{m_0} = C_{m_{0_{wb}}} + C_{L_{0_{wb}}}(h - h_{wb}) - C_{L_{0_{ht}}} \frac{l_t S_{ht}}{\bar{c}\, S} \quad \textbf{(4.9)}$$

$$C_{m_\alpha} = C_{L_{\alpha_{wb}}}(h - h_{wb}) - C_{L_T}\eta_{ht} \frac{l_t S_{ht}}{\bar{c}\, S} \quad \textbf{(4.10)}$$

$$C_{L_T} = (\, C_{L_{\alpha_{ht}}}(\alpha - \alpha \frac{\partial \varepsilon}{\partial \alpha} + \delta_e - \varepsilon_0) + \delta_{e,TR} C_{L_{ht,\delta_{e,TR}}}) \quad \textbf{(4.11)}$$

The same procedure for variable separation was applied to the pitching moment equations to isolate the wing-body pitching moment coefficient $C_{m_{0_{wb}}}$ and the pitching moment slope $C_{m_{\alpha_{wb}}}$.

4.2. Modelling single-slotted flaps

To ensure accurate modelling of the PA-28's flaps aerodynamics measurement of the aircraft's flaps and other key components was performed. This involved carefully examining the flaps to confirm that they are indeed single-slotted (*Figure 2*), rather than the plain flaps assumed in Pedrazzini's model.

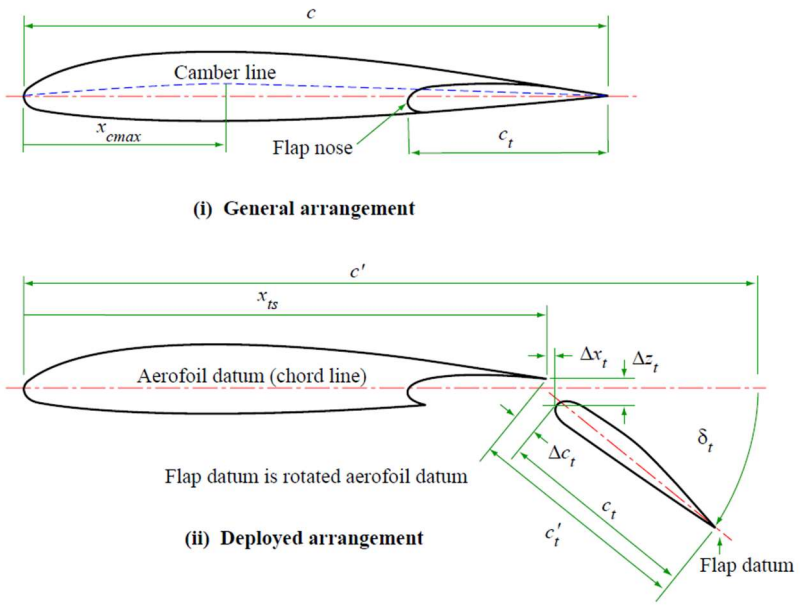

Figure 2 Single slotted flap sketch [20]

Additionally, the relative positions of important points, such as the wing quarter chord, flap position, and stabilator hinge, were measured relative to the body centreline. These measurements also incorporated in checking the twist of the wing, which plays a significant role in lift distribution and overall aerodynamics.

Table 1 Measurements done on PA-28

	Wing quarter chord	Flap trailing edge	Stabilator hinge	Twist
Distance from centreline	40 cm	61 cm	0 cm	-3°

Figure 3 shows a drawing of Piper PA-28-161 Warrior III, with centreline highlighted in red and measured dimensions in blue. It is important to note that the highlighted measurements are not up to scale, only for easier visualization.

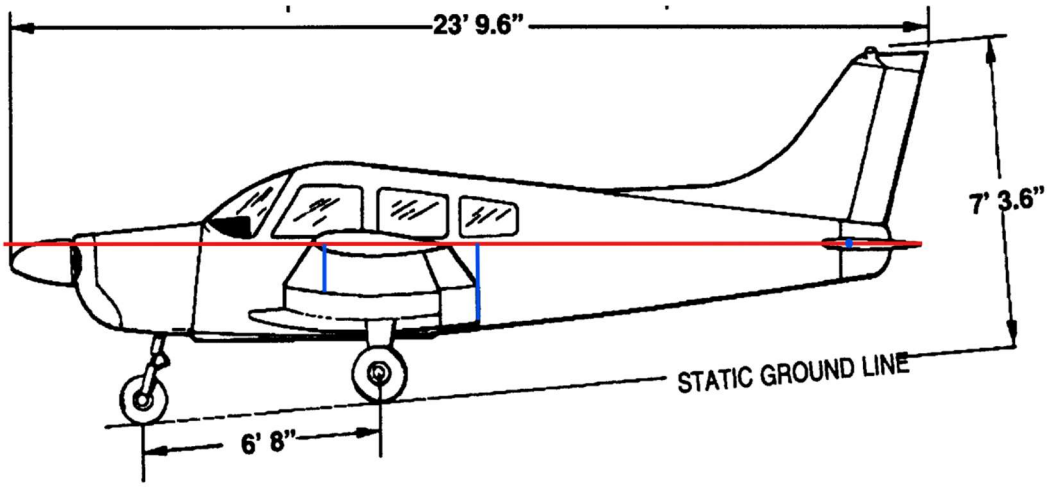

Figure 3 Piper PA-28-161 Warrior III side view [11]

4.2.1. Flaps lift

Methods described in ESDU were used to calculate the lift curve for a wing with part-span single-slotted flaps. ESDU 96003 [12] involves detailed steps to predict changes in lift up to maximum lift and captures the influence of flap deflection on overall lift behaviour. This calculation is structured to account for both the non-linear effects of lift increase due to flap deployment and the gradual onset of flow separation leading to stall.

The lift curve is evaluated in two individual parts, with the angle of attack α^* being the boundary between linear and nonlinear behaviour, as shown in *Figure 4*.

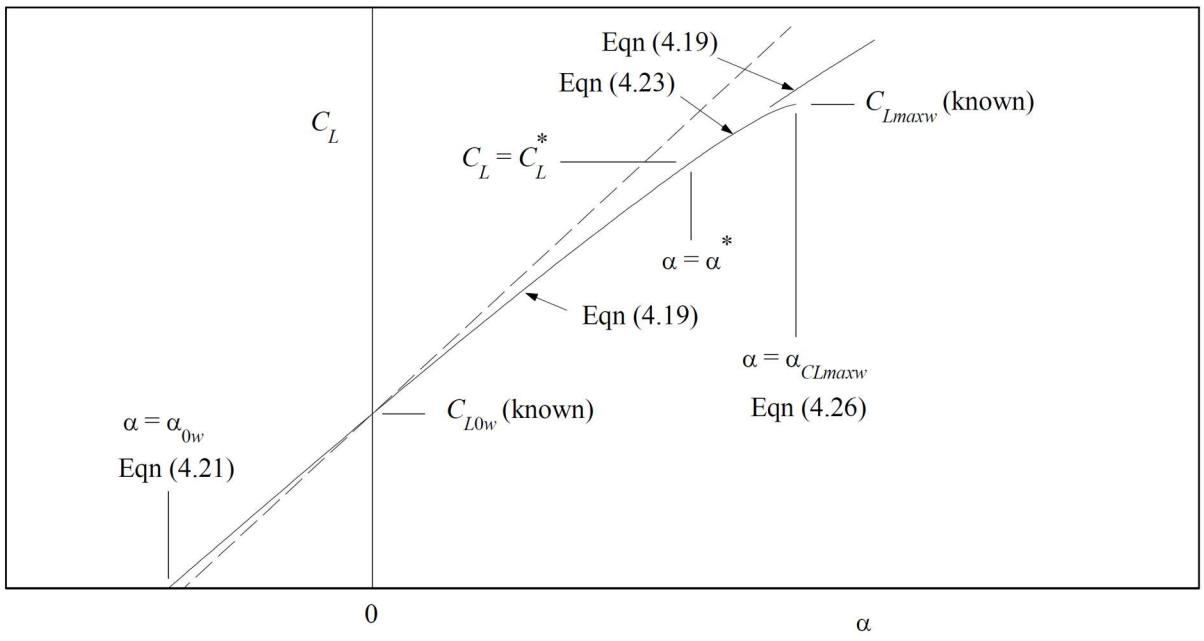

Figure 4 Lift curve with flaps - showing linear and non linear part [12]

The first part of the method described in ESDU 96003 [12] provides a linear estimate of the lift curve, starting from zero angle of attack up to the point where flow breakdown begins to significantly affect lift (Eq. 4.11).

$$C_L = a_1[1 + (\phi_0 - \phi_i)\left(\frac{\Delta c_t}{c} - \frac{K_\delta c_t}{c}\right)](\alpha - \alpha_{0w})cos^N(\alpha - \alpha_{0w}) \quad \textbf{(4.11)}$$

$$C_L = C_{Lmaxw} - (C_{Lmaxw} - C^*{}_L)[1 - \frac{a_1^*(\alpha - \alpha^*)}{p(C_{Lmaxw} - C_L^*)}]^p \quad \textbf{(4.12)}$$

The second part of the method provides a non-linear estimate of the lift curve (eq. 4.12), extending the estimation from $C_L{}^*$ to the point of maximum lift. This non-linear section predicts the angle of attack for maximum lift, considering flow separation and stall effects that disrupt the linear relationship between lift and angle of attack.

To follow the methodology outlined in ESDU 96003 [12] for estimating the lift curve of wings with high-lift devices, several additional ESDU files were used.

For the aerofoil-specific data, ESDU 94026 [13] was used to introduce methods for estimating lift coefficients at zero angle of attack and at maximum lift for aerofoils equipped with high-

lift devices, especially relevant at low speeds. Additionally, ESDU 84026 [14] provided the maximum lift coefficient for aerofoils at low Mach numbers up.

For basic wings without flaps, ESDU 70011 [15] was used to determine the basic wing lift-curve slope, ESDU 89034 [16] was used to estimate the maximum lift for a plain wing, and ESDU 87031[17] was used to calculate the wing's angle of attack at zero lift for subcritical Mach numbers.

Finally, for wings with flaps, several ESDU files addressed specific lift increments. ESDU 93019 [18] provided the lift coefficient increment at zero angle of attack for wings with flaps deployed and ESDU 91014 [19] covered maximum lift for wings equipped with single-slotted flaps.

4.2.2. Flaps drag

Starting with the lift curve of the wings with deployed flaps, calculated in the previous chapter using ESDU 96003 [12] and including adjustments for part-span single slotted flap effects, the drag curve of the PA-28 wings with deployed flaps is calculated.

To calculate the increment in wing profile drag coefficient due to the deployment of single-slotted flaps, ESDU 08013 [20] provides a detailed method that separates lift-independent and lift-dependent drag contributions. This approach captures how flap deployment alters the aerofoil and wing drag characteristics.

The process begins with the aerofoil's baseline drag polar in a clean configuration, focusing on the minimum drag coefficient and the associated lift coefficient. The drag components are determined using ESDU 06001 [21] for skin friction drag and ESDU 00027 [22] for profile drag, both applicable to Mach numbers below the drag-rise condition. Profile drag coefficient increment due to full-span single-slotted flaps is added using ESDU Aero F.02.01.06. [23].

The flap-specific drag contributions are calculated based on ESDU 08013 [20], which accounts for the additional drag due to flap deflection and the part-span nature of the flaps. To model the spanwise effects, ESDU F.02.01.08 [24] provides the vortex drag coefficient for wings with part-span flaps and central cutouts. This allows for precise adjustment of the drag profile to account for the non-uniform lift distribution caused by the flaps.

Finally, corrections for viscous drag in shock-free attached flow were applied using ESDU 07002 [25], ensuring the drag calculation reflects realistic flow conditions.

4.2.3. Flaps pitching moment

The ESDU 03017 [26] document provides a method to predict the pitching moment curve for wings with high-lift devices at low speeds, such as the single-slotted flaps on the PA-28 aircraft. The process starts with calculating the clean wing's aerodynamic characteristics, including lift and pitching moment coefficients. For the PA-28, ESDU 72024 [27] was used to determine the aerodynamic properties of the aerofoil in compressible, inviscid flow at subcritical Mach numbers.

The lift characteristics of the PA-28 wing, calculated earlier using ESDU 96003 [12], were used as a basis to estimate the effects of flap deployment on the pitching moment. Flap deployment affects the pitching moment by altering the lift distribution and shifting the aerodynamic centre. These changes were calculated using ESDU 99004 [28], which provides methods for determining the pitching moment coefficient at zero angle of attack for trailing-edge single-slotted flaps.

4.3. Comparison and validation of results using XFLR5

4.3.1. ESDU Results

The results for the longitudinal aerodynamic coefficients of the PA-28 wing, in both the clean configuration and with flaps deployed at 10°, 25°, and 40°, were calculated using ESDU methods described in the previous chapter. These graphs show the wing performance with different flap settings as a function of angle of attack.

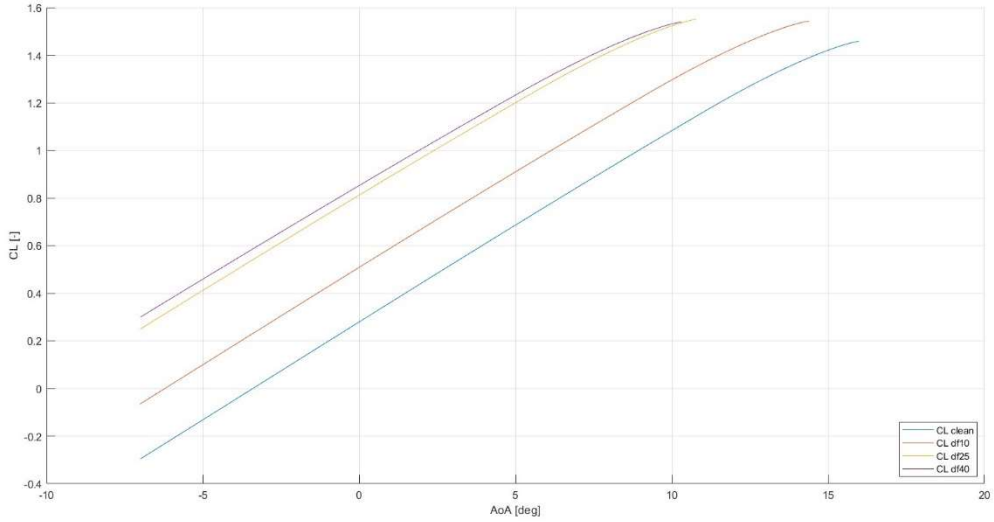

Figure 5 PA-28 wing lift coefficient – ESDU results

The graph in *Figure 5* shows the lift coefficient. The C_L curves extend up to their respective maximum lift coefficients $C_{L_{max}}$. As expected, flap deflections at 10° and 25° show a significant increase in lift compared to the clean configuration, with a smaller gain observed for the 40° flap deflection than for 25°. This makes sense, as the 40° flap position is mainly used during landing, where managing descent and speed is more important than generating extra lift.

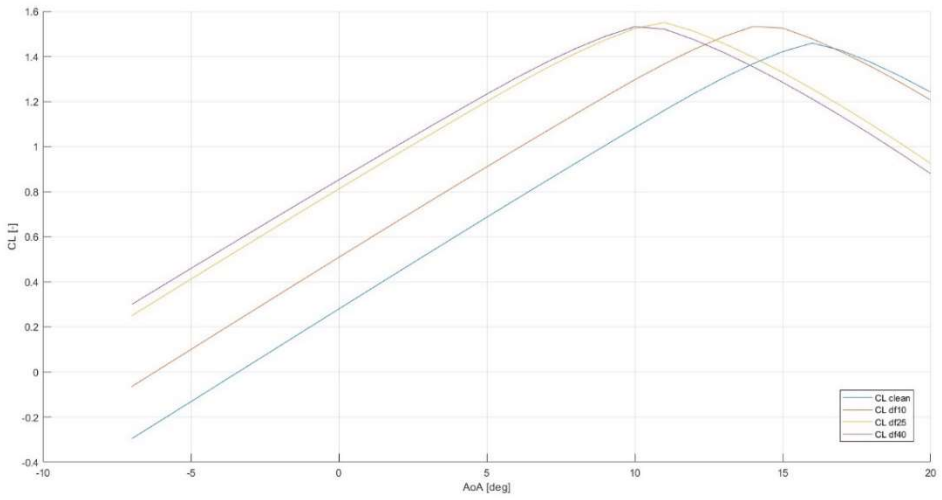

Figure 6 PA-28 wing lift coefficient - extended curve – ESDU results

The graph in *Figure 6* shows extended lift coefficient curves beyond $C_{L_{max}}$ into the stall region by modifying equations from ESDU 96003 [12]. This extension was done to ensure the simulator model behaves smoothly instead of having a sudden cut-off at $C_{L_{max}}$. However, it is important to note that this does not represent the true stall behaviour of the wing, as modelling stall is outside the scope of this thesis.

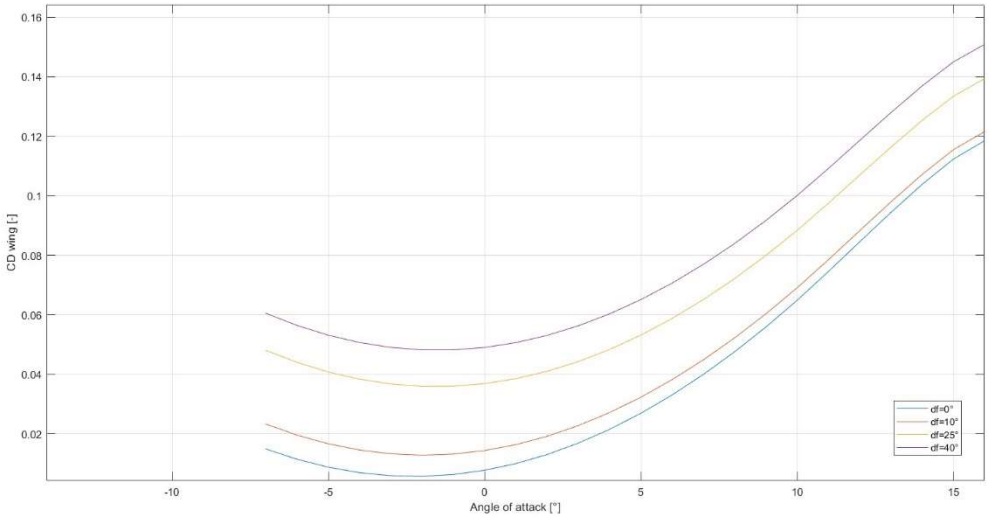

Figure 7 PA-28 wing drag coefficient – ESDU results

The graph in *Figure 7* shows the drag coefficient C_D for the different flap settings. The results indicate a small increase in drag for the 10° flap deflection, but a much larger rise for 25° and 40°. This aligns with expectations, as flaps at 40° significantly increase drag, even though the lift gain is relatively small. This reflects the primary purpose of the 40° flaps, which is to add drag and help control speed during landing.

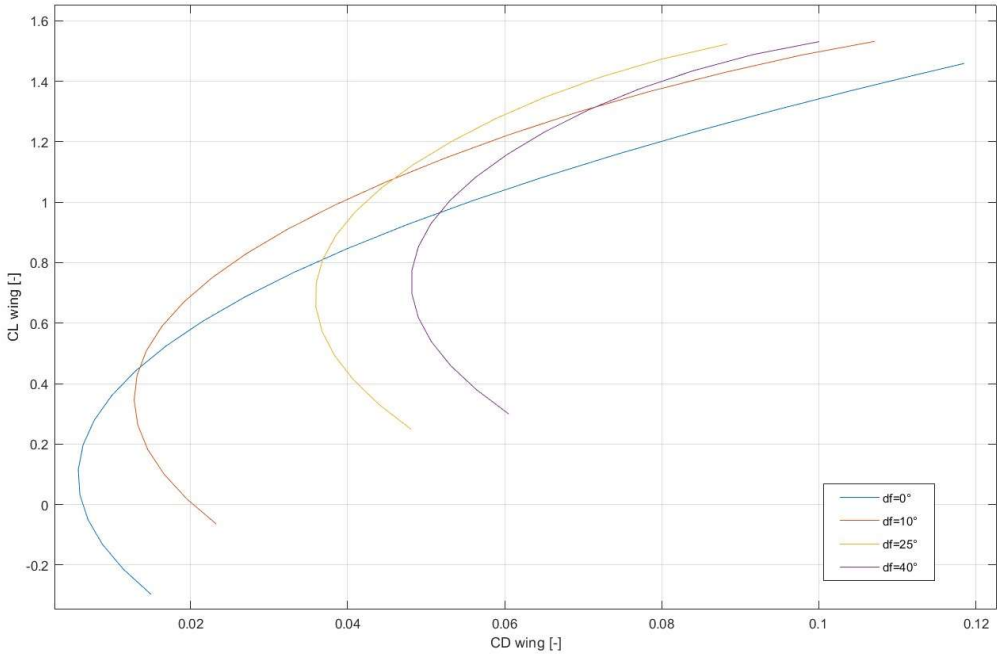

Figure 8 PA-28 wing drag polar – *ESDU results*

Flap deployment introduces two main effects: a lift-independent drag increase from the flap deflection angle and geometry, and a lift-dependent drag increment due to the additional lift generated, especially at higher angles of attack. These changes also shift the drag polar *(Figure 8*), increasing the minimum drag coefficient and altering the lift coefficient at minimum drag.

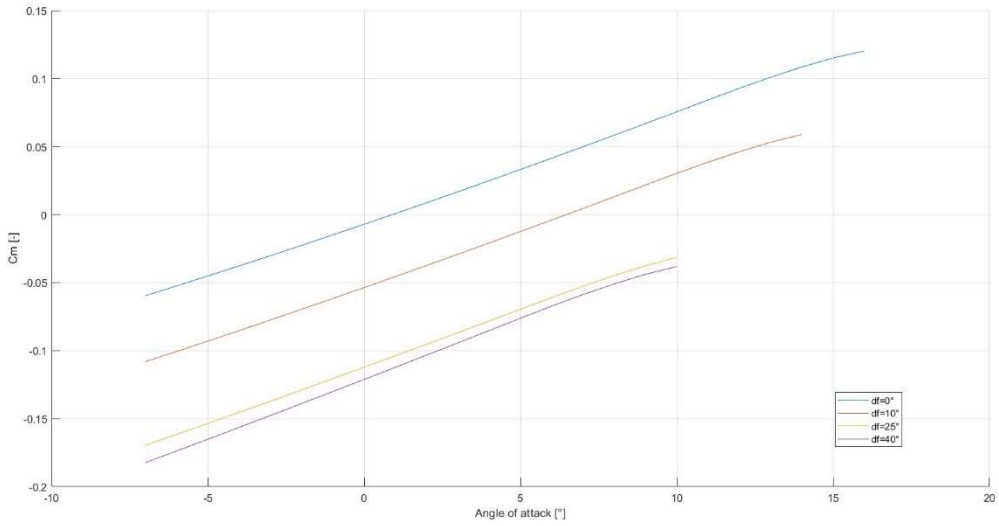

Figure 9 PA-28 wing pitching moment coefficient – ESDU results

The graph in *Figure 9* shows the pitching moment coefficient C_m across angles of attack. The wing shows static aerodynamic instability in pitch, as the C_m increases with angle of attack, causing a "nose-up" rotation. Flap deflections at 10° and 25° result in a larger increase in C_m compared to 40°. This is expected considering the principle that the pitching moment results from the lift force acting at a given lever arm, with its magnitude directly influenced by the lift increment.

4.3.2. XFLR5 comparison

XFLR5 is a software tool designed for analysing airfoils, wings, and aircraft operating at low Reynolds numbers. It incorporates XFoil's direct and inverse analysis features, as well as wing design and analysis capabilities using methods like lifting line theory, vortex lattice method (VLM), and a 3D panel method [29].

In this thesis, XFLR5 was used to validate the results derived in the previous chapters.

XFLR5 cannot model single-slotted flaps accurately because it does not account for the slot aerodynamics, like delayed airflow separation, that increase lift. For this reason, XFLR5 uses plain flap approximations instead, simplifying the calculations.

Wing modelled in XFLR5 is shown in two perspectives, *Figure 10* in isometry and in *Figure 11* rotated to highlight flaps:

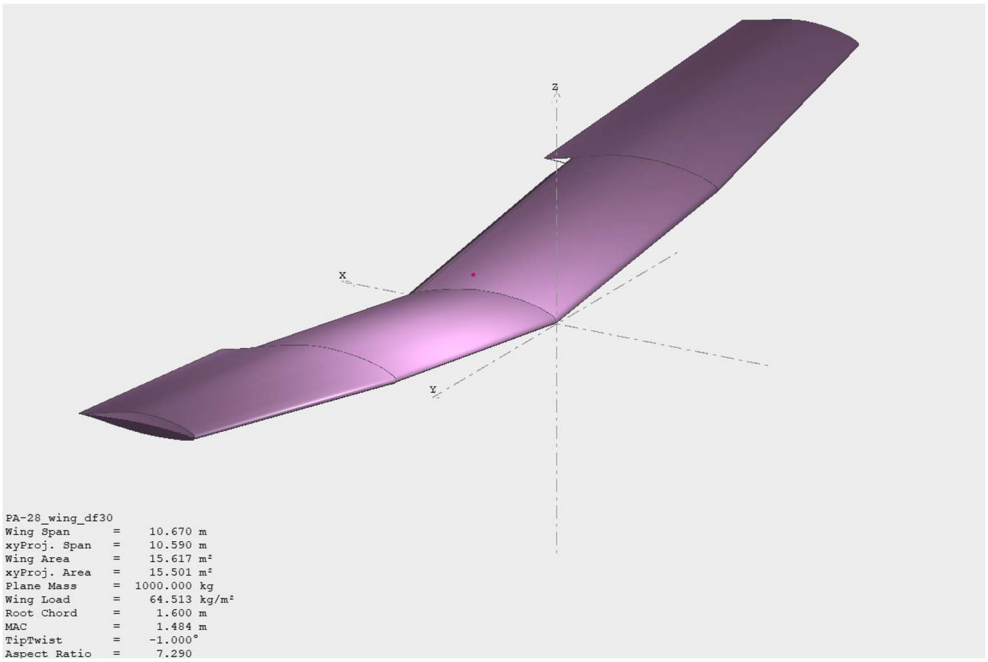

Figure 10 Wing modelled in XFLR5 - isometry

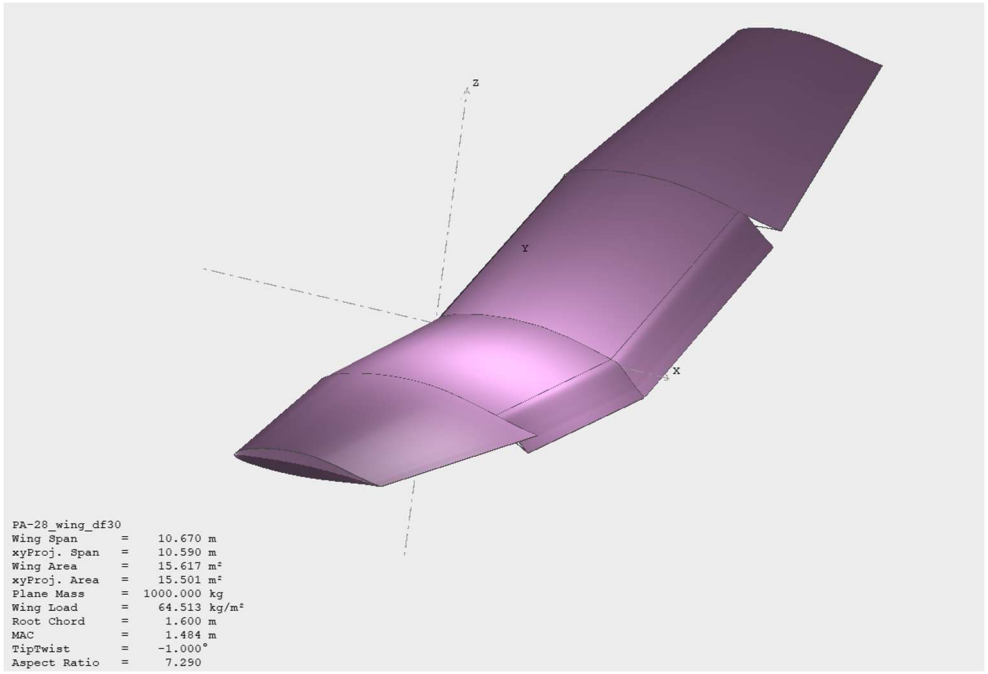

Figure 11 Wing modelled in XFLR5 - rotated to highlight flaps

By implementing the VLM method, XFLR5 analysis produces the following results (*Figure 12*) for lift, drag and pitching moment coefficient as a function of angle of attack (AoA). The graphs are arranged in the figure as follows: the top left shows C_D over AoA, the top right shows C_L over AoA, the bottom left shows C_m over AoA, and the bottom right shows C_L/C_D over AoA.

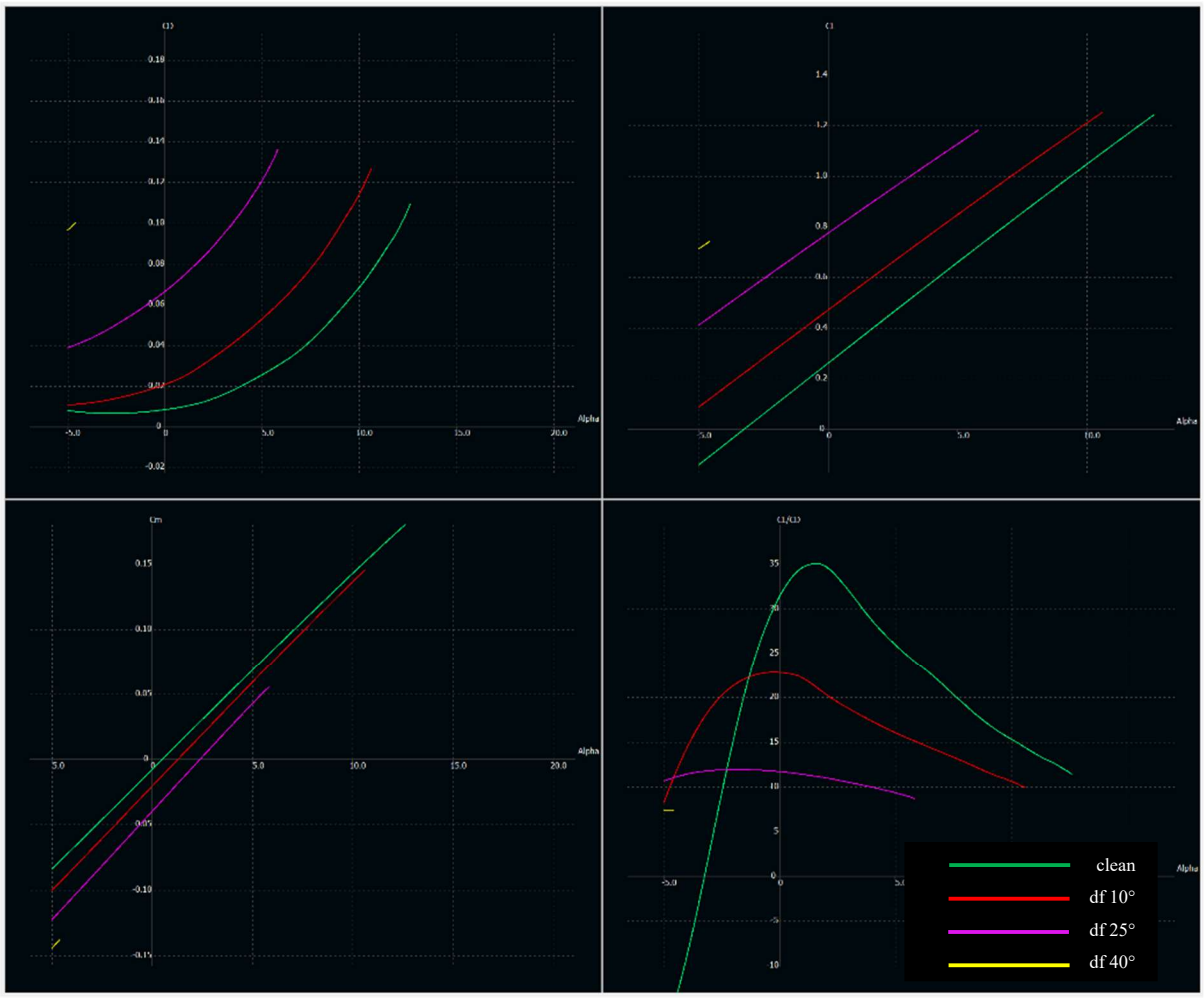

Figure 12 XFLR5 analysis results

Lift comparison

The graph in *Figure 13* compares lift coefficient results from ESDU (solid lines) and XFLR5 (dashed lines) for different flap configurations. For the clean configuration and configurations with flaps deployed at 10° and 25°, the results align well. Both the lift increments due to flap deflection and the lift curve slopes match closely between ESDU and XFLR5.

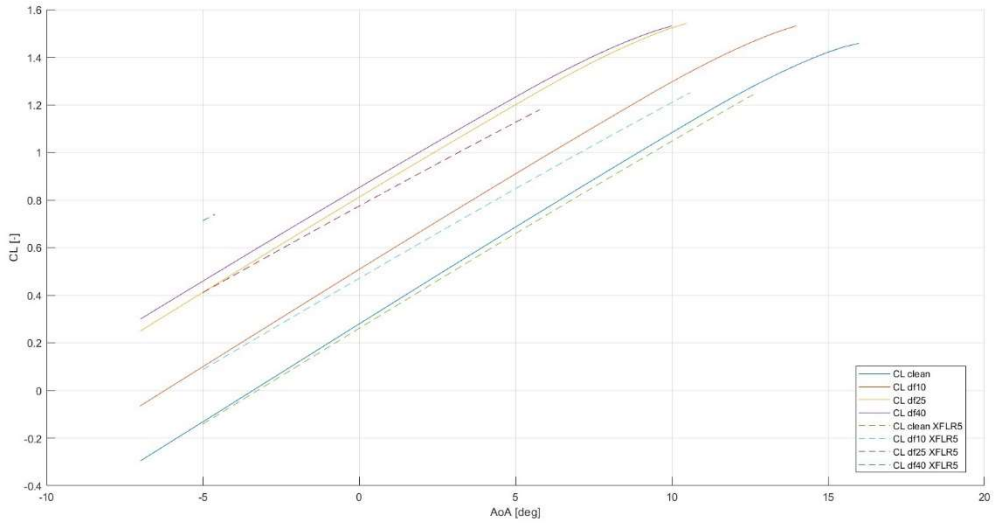

Figure 13 Wing lift results - ESDU and XFLR5 comparison

However, the results for the 40° flap deflection configuration show significant discrepancies. In this case, XFLR5 produced only two data points, which do not align with the results given by the ESDU method. This inconsistency is likely due to numerical instability within XFLR5's calculations. The software relies on iterative solvers which can fail to converge under certain conditions, especially when dealing with high flap deflection angles. Additionally, as an open-source tool, XFLR5 occasionally exhibits bugs that lead to glitches or unexpected behaviour during certain configurations [29].

Despite these issues, the maximum angle of attack where the lift coefficient stays linear α^* matches well between the ESDU method (calculated in Section 4.2.1) and XFLR5. This is shown in *Table 2* to confirm that both methods give similar results for the linear part of the lift curve.

*Table 2 Comparison of ESDU and XFLR5 results for α**

δ_f°	0°	10°	25°	40°
ESDU* α	10.99°	9.29°	5.70°	5.10°
XFLR5 α*	12.6°	10.5°	5.8°	/

Drag comparison

The two graphs (*Figure 14* and *Figure 15*) compare drag coefficient predictions from the ESDU method and XFLR5 for different flap deflections. For the clean configuration, both methods

match well on the zero-lift drag coefficient C_{D0}. However, significant differences emerge as the angle of attack increases. XFLR5 predicts a much steeper rise in drag compared to ESDU, particularly for higher flap deflections.

XFLR5 also predicts the change in the angle of attack for C_{D0} when flaps are deployed, while the ESDU method does not. In this regard, XFLR5 provides a more accurate representation, as C_{D0} does change with flap deployment. When flaps are deployed, the airfoil's camber and chord are altered, causing the wing to generate lift at a lower angle of attack compared to a clean configuration. As a result, C_{D0} for flaps should occur at lower angles of attack, as shown in the XFLR5 results.

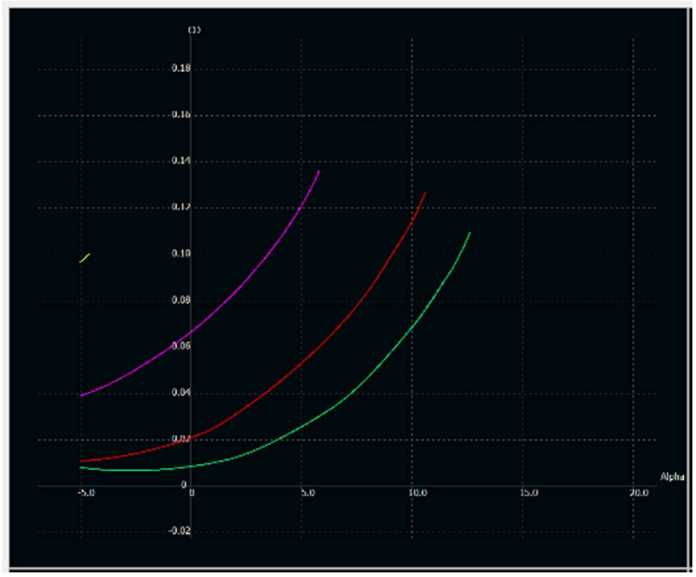

Figure 14 Wing drag results XFLR5

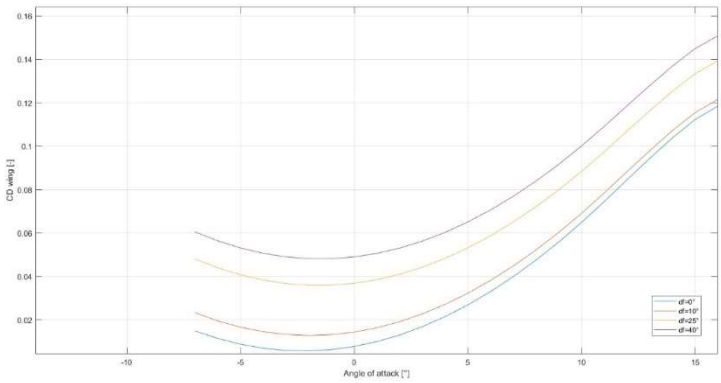

Figure 15 Wing drag results ESDU

These discrepancies can be attributed to limitations in XFLR5's drag calculation methods, as XFLR5 uses VLM to estimate drag. While it calculates lift-induced drag reasonably well under assumptions of elliptical lift distribution, it struggles with complex geometries such as taper, twist and the aerodynamic effects of flaps [29]. Additionally, form drag, influenced by the wing and fuselage geometry, is also not explicitly modelled in XFLR5, whereas the ESDU method incorporates these contributions, including central cutouts in flap and wing to account for fuselage [24]. Another significant difference is that the ESDU method considers viscous effects [25], making it more accurate for real-world drag predictions.

One notable similarity is how both methods capture trends in drag increment due to flap deflection. For a 10° flap deflection, both ESDU and XFLR5 predict a small increase in drag. However, the drag increases significantly for 25° flap deflection, showing a similar pattern in the magnitude of jumps for both of these configurations. This highlights a consistent prediction of how flaps influence drag, despite XFLR5's limitations in absolute drag prediction.

Pitching moment comparison

The two graphs (*Figure 16* and *Figure 17*) compare pitching moment coefficient predictions from the ESDU method and XFLR5 for varying flap deflections.

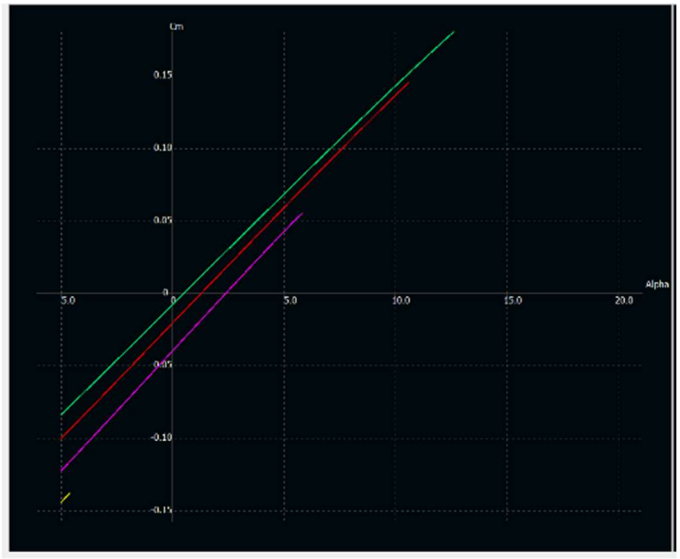

Figure 16 Wing pitching moment results XFLR5

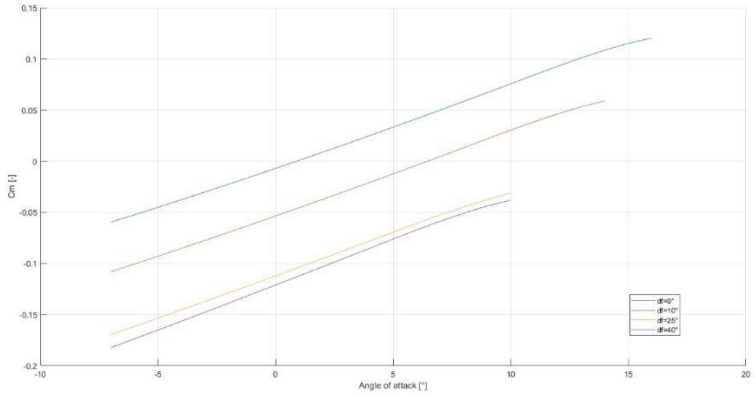

Figure 17 Wing pitching moment results ESDU

Both graphs indicate that the wing is unstable, as evidenced by the increase in the pitching moment coefficient C_m with the angle of attack. As expected, flap deflection consistently results in a downward shift of the pitching moment coefficient across all angles of attack, aligning with aerodynamic principles.

XFLR5 displays less reliable results, with much steeper pitching moment curve slope and deviations that become more noticeable at higher angles of attack. This is primarily due to previously mentioned limitations in XFLR5's simulation methods. Furthermore, errors in calculating the centre of gravity position relative to the aerodynamic centre can distort the analysis [29].

The lift results are promising, as both ESDU and XFLR5 provide similar predictions. This consistency gives a strong foundation for further modelling, with lift coefficient calculations from ESDU 96003 [12] forming the base for the drag and pitching moment models. Although XFLR5 has some accuracy issues, it still shows consistent trends in how flaps affect drag and pitching moment, matching the overall patterns seen in ESDU.

In conclusion, ESDU documents are more dependable for precise aerodynamic coefficients due to their validated methods. However, XFLR5 is still useful for understanding trends and parameter sensitivities, and providing rough estimates, even if it is less reliable for exact values. Therefore, the values for the aerodynamic coefficients calculated using ESDU methods will be used further in the model.

5. DOWNWASH MODELING

Understanding and calculating downwash is critical for flight simulation and stability and control analysis. It helps determine how the wing's lift affects the tailplane's angle of attack and pitching moment. This is particularly important in optimizing the interaction between the wing and the tailplane for improved performance and stability.

Downwash is the downward velocity imparted to the air by a wing as it generates lift. This downward motion occurs because the wing interacts with the surrounding air, deflecting it downward. As the wing moves through the air, it forms a "tube" of downwashed air behind it, where the vertical velocity of this airflow is referred to as downwash *w* (*Figure 18*) [30].

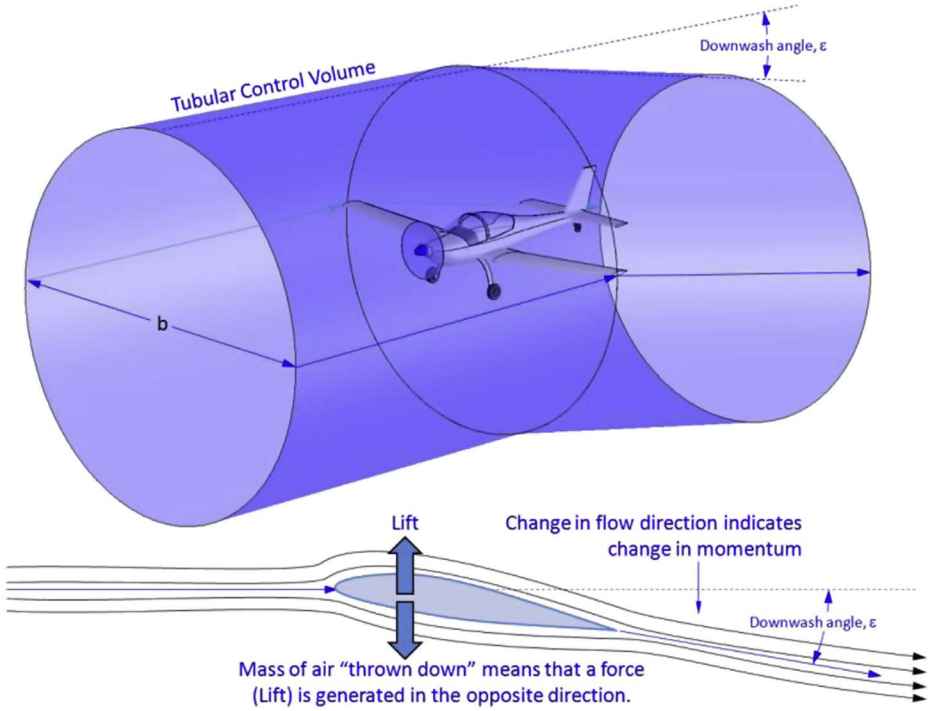

Figure 18 Downwash [30]

The lift produced by the wing can be linked to this downwash using Newton's Second Law (Eq 5.1) where ṁ is the mass flow rate of the deflected air. By assuming the diameter of this stream tube equals the wingspan *b*, the momentum change from downwash provides a reliable estimation of the lift force, followed by an expression for downwash (Eq. 5.2, 5.3) [30].

$$L = \dot{m}w = \rho\left(\frac{\pi}{4}\right) b^2 V w \tag{5.1}$$

$$L = \frac{1}{2}\rho V^2 S C_L \leftrightarrow w = 2V\left(\frac{S}{\pi b^2}\right)C_L \quad \textbf{(5.2)}$$

$$w = \frac{2C_L}{\pi A}V \quad \textbf{(5.3)}$$

Since the downwash can be expressed as the vertical component of velocity, with $\sin(\varepsilon)$ approximated as ε, then the downwash angle ε, represents the tilt of the airflow due to downwash (Eq. 5.4-5.5) [30].

$$w = \varepsilon V \quad \textbf{(5.4)}$$

$$\varepsilon = \frac{2C_L}{\pi A} \quad \textbf{(5.5)}$$

The downwash angle ε increases with the lift coefficient C_L, altering the angle of attack experienced by the tailplane. This change in downwash influences the tailplane's effectiveness and the overall stability of the aircraft, especially in high-lift configurations.

Equations (5.6) and (5.7) for the downwash gradient and downwash angle at zero angle of attack follow [30].

$$\frac{d\varepsilon}{d\alpha} = \frac{2}{\pi A}\frac{d}{d\alpha}\left(C_{L_0} + C_{L_\alpha}\alpha\right) = \frac{2C_{L_\alpha}}{\pi A} \quad \textbf{(5.6)}$$

$$\varepsilon_0 = \frac{\partial \varepsilon}{\partial \alpha}\alpha_{0wb} \quad \textbf{(5.7)}$$

5.1. Choice of method

This method described by S. Gudmundsson was chosen for its simplicity, although other were used for validation purposes.

Results for downwash gradient using other methods shown in Table 3:

Table 3 Downwash gradient comparison

	S. Gudmundsson	Etkin and Reid	New Method	ESDU 80020
$\frac{d\varepsilon}{d\alpha}$	0.4440	0.4488	0.4068	0.5199

5.1.1. Etkin and Reid

The method from Etkin and Reid's *Dynamics of Flight* [31] uses data from the USAF Datcom. While this method also accounts for wing aspect ratio, wing taper ratio, and tail position, it

relies on empirical coefficients derived from wind tunnel tests. These coefficients can introduce uncertainty, as they may not apply to all configurations.

5.1.2. A New Method for the Prediction of the Downwash Angle Gradient

Another method [32], developed by Dr. Mondher Yahyaoui, is based on a method in Raymer [33], but with improved accuracy by estimating coefficients using the Vortex Lattice Method. This method considers the wing aspect ratio, taper ratio, and tail position, sweep and twist.

5.1.3. ESDU

The ESDU 80020 [34] method is the most detailed and considers multiple factors, such as wing aspect ratio, taper ratio, tail position, and sweep angles at the quarter-chord and mid-chord points of the wing. While this makes it more comprehensive, it can also lead to inaccuracies, due to difficulties in interpreting some of the required figures.

5.2. Downwash angle for wings with deployed flaps

In this thesis, NACA Report No. 648 [35] was used to calculate the downwash angle behind the wing with deployed flaps.

In the report a more complex approach is explained, using the tailing vortex sheet behind the wing, instead of the air "tube" explained by S. Gudmundsson in the previous chapter [30].

Downwash here refers to the downward airflow produced by the vortex system of a wing as it generates lift. For a plain wing, this vortex system consists of a bound vortex along the quarter-chord line and a trailing vortex sheet extending downstream from the trailing edge. The trailing vortex sheet is displaced downward due to the airflow induced by the wing itself. The strength of this vortex system is directly proportional to the lift coefficient C_L, which means the downwash angle ε and the vertical displacement of the sheet h also increase with C_L. At higher lift conditions, additional factors, such as tip vortices and wake interactions, also influence the downwash pattern [35].

The calculation of downwash begins with the plain wing, for which the trailing sheet is shed at the trailing edge. The trailing vortex sheet is initially treated as a system of idealized horseshoe vortices extending downstream (*Figure 19*). This approach assumes the sheet is uniformly displaced downward near the tailplane h_1, simplifying the calculation of the downwash angle. This method effectively captures the primary effects of the vortex system without requiring complex deformation modelling of the trailing sheet [35].

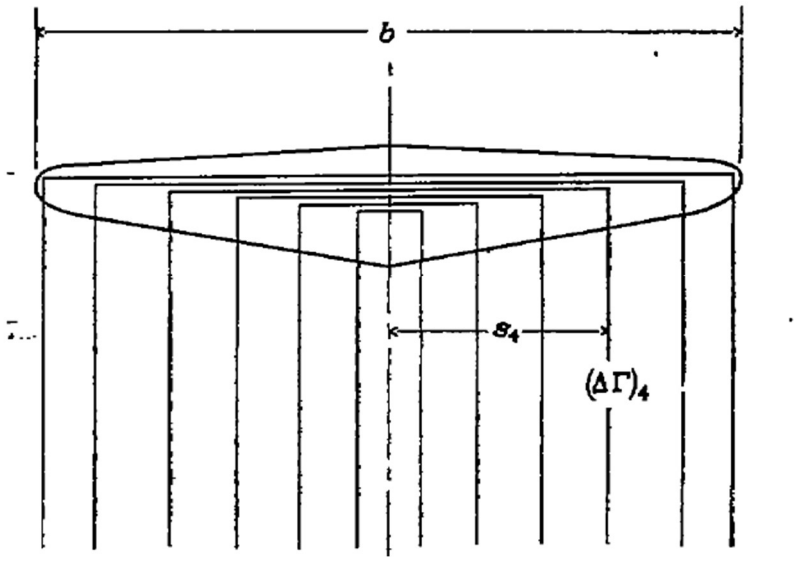

Figure 19 The trailing vortex sheet as a system of idealized horseshoe vortices [35]

When flaps are deployed, the spanwise lift distribution changes significantly, which alters the downwash. The vortex sheet in a flapped wing originates between the trailing edges of the wing and the flap *m*, and its displacement reflects the combined influence of the plain wing and flap (*m+h1+h2*). The extra lift generated by the flap is proportional to the flap's contribution to downwash, which adds to the downwash effect of the plain wing [35].

Downwash charts provided in the NACA report no. 648 [35] (*Figure 20*) are used to represent the calculated results for spanwise loading distributions and downwash angles for different configurations. The given results differ depending on wing planform, aspect ratio, taper ratio and flap span.

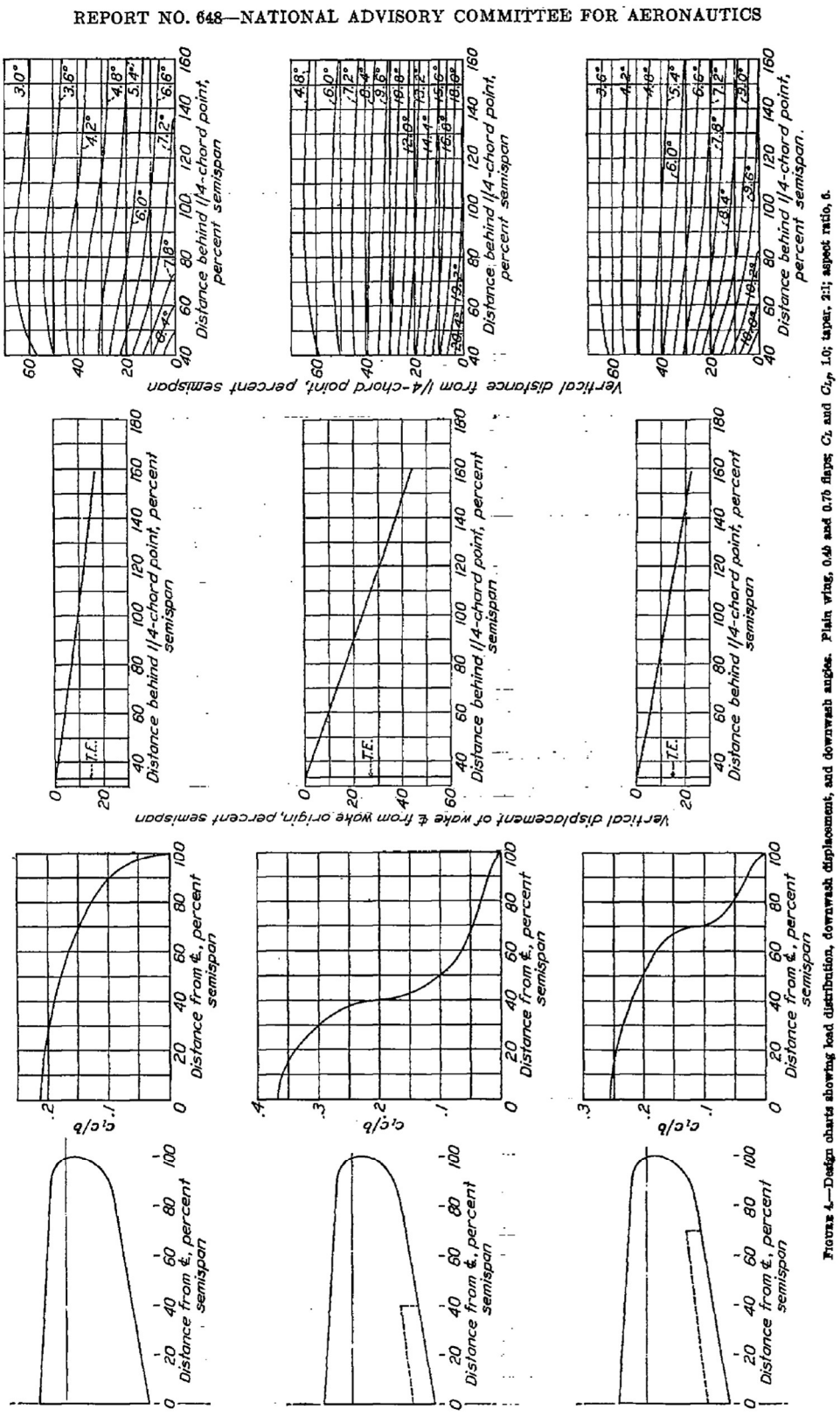

FIGURE 4.—Design charts showing load distribution, downwash displacement, and downwash angles. Plain wing, 0.4b and 0.7b flaps; C_L and C_{l_p} 1.0; taper, 2:1; aspect ratio, 6.

Figure 20 Charts provided in NACA report no.648 [35]

The charts assume idealised conditions, such as a quarter-chord line perpendicular to the centreline and provide a clear visual guide for interpreting the effects of plain and flapped wings. Practical deviations, such as non-uniform flap chords or wing-tip effects, are accounted for through additional corrections given in the report to ensure the calculations remain applicable to real-world scenarios [35].

The method described in the report is sensitive to the angle of attack, which influences the contributions of the wing and flap to the overall downwash and the relative positioning of the wake [35].

The process for calculating the downwash for a wing with deployed flaps involves several steps [35].

1. The downward displacement of airflow h is divided into contributions from the plain wing and the flap. For the plain wing, the displacement h_1 depends solely on the wing configuration and position. For the flap, charts are used to determine the displacement contribution based on the flaps lift coefficient increment and its relative spanwise position x. This is repeated to calculate the flaps contribution, h_2 to the total displacement.
2. The origin of the wake m is determined using equations and reference charts detailed in the report. It accounts for factors such as flap deflection angle and wing/chord ratio. The wake's downward displacement is influenced by both the wing and flap contributions. The combined displacement ($h=h1+h2$) is used to locate the wake relative to the tailplane.
3. The downwash contributions from the wing and flap are calculated separately. Charts provide the values for the downwash angle at the tailplane location, which is defined by the coordinates (x, $h1$) for a plain wing and (x, $h+m$) for a wing with flaps deployed. The contributions are proportional to the respective lift coefficients of the wing and flap and are summed to find the total downwash angle ε.
4. Interpolation between graphs for flap span and aspect ratio of PA-28 was performed (*Figure 21*). After that, the correction factor for variation of downwash across the tail span was applied and values of total downwash angle ε were sized to CL value at a given angle of attack.

5. Since the model already included the downwash gradient for a plain wing, only the additional increment caused by the flaps needed to be added. To do this, the total downwash angle from the previous step was adjusted by subtracting the downwash angle of the plain wing, which was sized for a specific lift at a given angle of attack. This provided the contribution to the downwash caused by the deployed flaps.

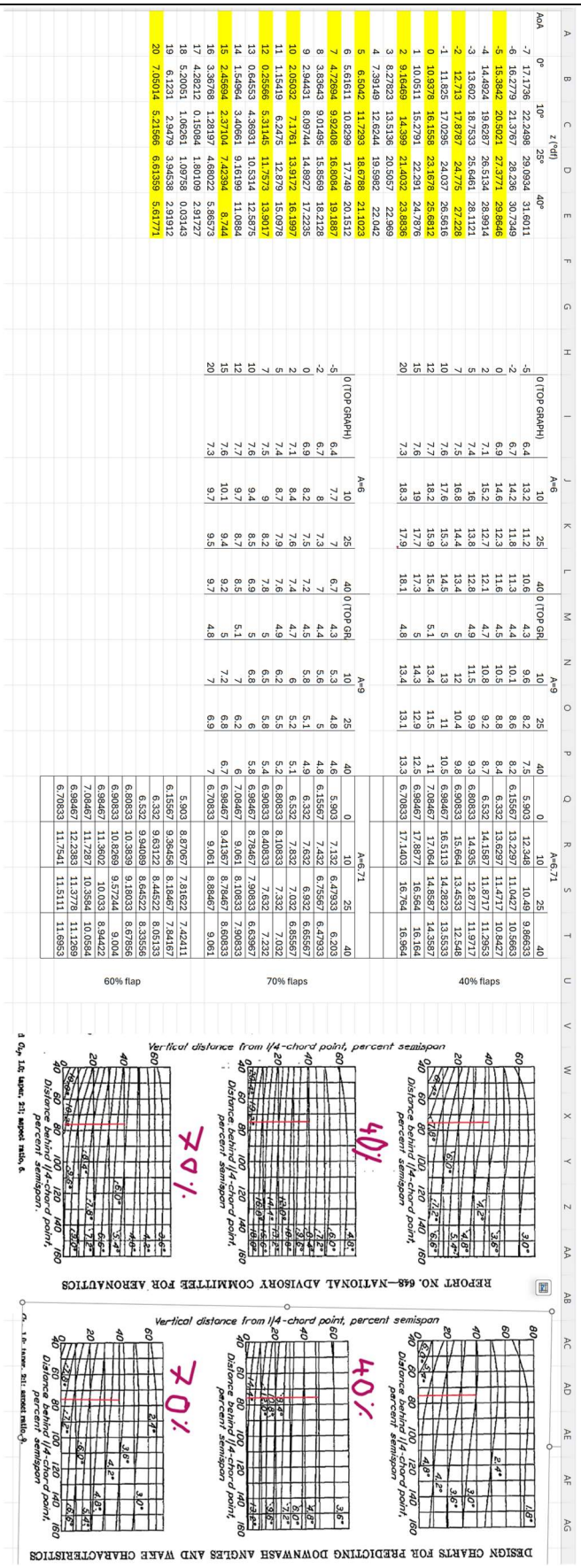

Figure 21 Downwash angle interpolation

5.3. Dynamic pressure loss

The wake's characteristics analysis, such as pressure loss and turbulent mixing, are included in the NACA report no.648 [35]. These effects are particularly important for wings with flaps, as they influence the vortex sheet's behaviour and the resulting downwash.

The wake, which aligns with the centre of the trailing vortex sheet, experiences a loss of total pressure proportional to the profile drag of the wing section. As turbulent mixing occurs downstream, the wake widens, and the pressure loss decreases, although the total integrated loss remains constant [35].

If the wing and tail are positioned such that the tail lies within the wake, as shown in *Figure 22*, the average reduction in dynamic pressure at the tail must be taken into account. The dynamic pressure loss at the hinge axis is often used as an approximation for this value, although it may differ slightly from the average across the entire tail surface. Whether the tail lies within the wake or not depends on the angle of attack, which determines the position of the tail relative to the wing, responsible for generating the wake [35].

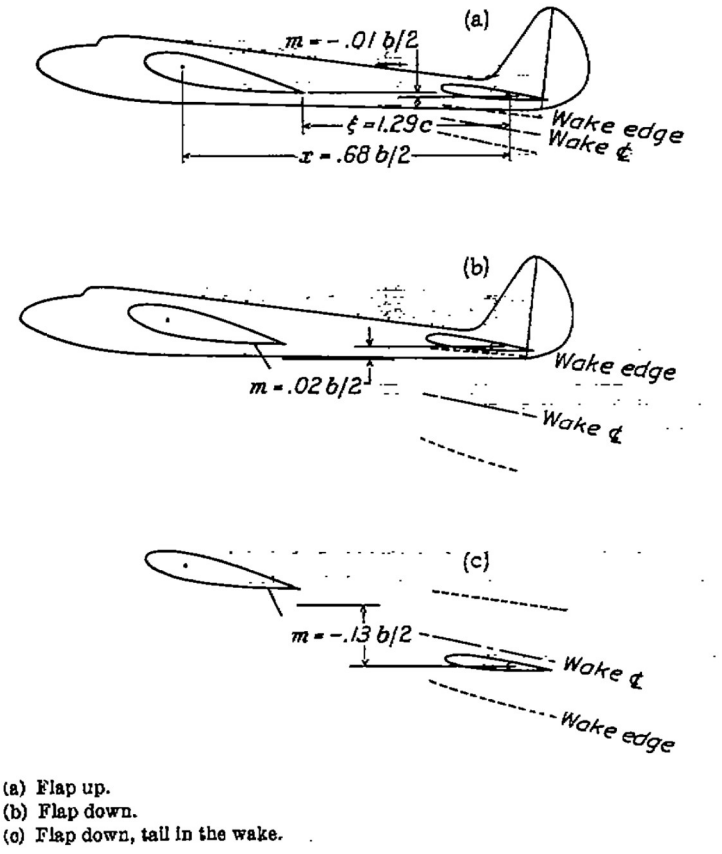

(a) Flap up.
(b) Flap down.
(c) Flap down, tail in the wake.

Figure 22 Wing wake and tailplane relation [35]

The following steps [35] describe the process for calculating the dynamic pressure at the tailplane:

1. To determine the vertical displacement (h+m), results from the downwash angle calculation in the previous chapter were used, alongside the wake width ζ per equation (5.8), as the kinetic pressure at the tailplane depends on the distance from the trailing edge ξ and the position of the tail in regards to the wake.
2. Calculation of the maximum pressure loss and the distribution of dynamic pressure in the wake is given by the equations (5.9) and (5.10)
3. Dynamic pressure at a given point depending on angle of attack is given by equation (5.11)

$$\zeta = 0.68\sqrt{c_{d0}(\xi + 0.15)} \tag{5.8}$$

$$\eta = \frac{2.42{c_{d0}}^{1/2}}{\xi + 0.3} \tag{5.9}$$

$$\frac{\eta'}{\eta} = cos^2(\frac{\pi}{2}\frac{\zeta'}{\zeta}) \tag{5.10}$$

$$\eta_p = 1 - \eta' \tag{5.11}$$

5.4. Results

The first graph in *Figure 23* shows the total downwash angle behind the wing in clean configuration and with flaps deployed at 10°, 25°, and 40°.

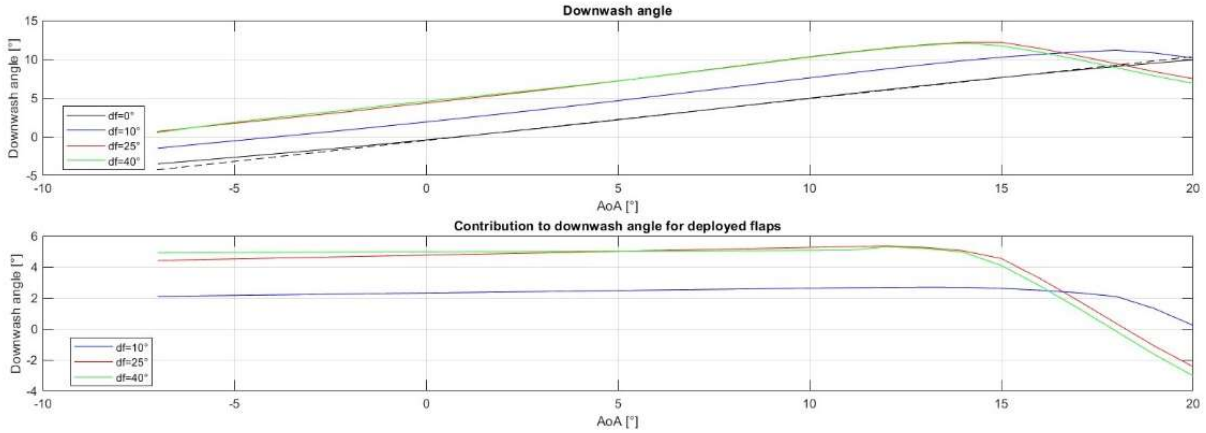

Figure 23 Downwash angle

The downwash angle curve closely mimics the lift curve, as expected, since it is directly influenced by the lift generated by the wing. With increasing flap deflection, the downwash angle increases due to the added lift from the deployed flaps.

The second graph in *Figure 23* focuses on the increment in downwash angle caused by flap deployment. It can be observed that the increments for flap deflections of 10° and 25° result in a similar jump in downwash angle, while the 40° flap curve almost aligns with the 25° curve. This indicates that, despite the increased flap deflection, the additional lift generated between 25° and 40° flaps contributes very little to the downwash angle.

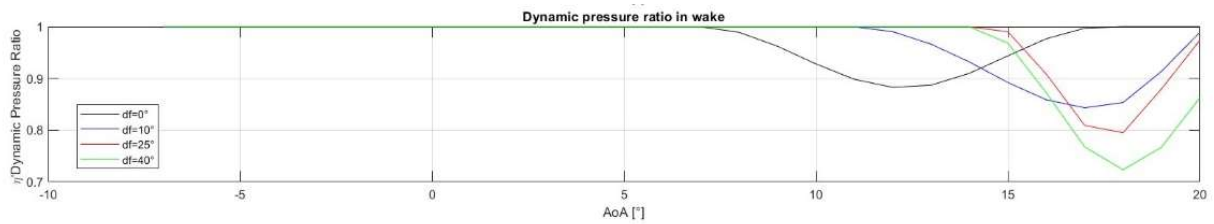

Figure 24 Dynamic pressure ratio in the wake

Figure 24 shows the dynamic pressure ratio at the tailplane. For low angles of attack, the tailplane remains unaffected by the wing's wake, resulting in no loss of dynamic pressure. As the angle of attack increases, the tailplane moves into the wing's wake, leading to a reduction in dynamic pressure.

The onset of dynamic pressure loss occurs at higher angles of attack for larger flap deflection angles. This is expected due to the greater downward displacement of airflow caused by larger flap deflections. Interestingly, while there is minimal difference in downwash angle between 25° and 40° flaps, the dynamic pressure loss at the tail is significantly different. For 25° flaps, the tail experiences ~20% pressure loss, while for 40° flaps, the loss approaches 30%. This highlights that higher flap deflections amplify wake effects, significantly affecting the aerodynamic efficiency of the tailplane.

5.5. Longitudinal aerodynamic model

Equations 38 and 39 show the new structure of the longitudinal aerodynamic model, with the parameters estimated in previous chapters: $C_{L_{0_{wb}}}$(*Section 4.1*) , $C_{L_{\alpha_{wb}}}$(*Section 4.1*), $C_{m_{0wb}}$ (*Section 4.1*), $C_{m_{\alpha_{wb}}}$(*Section 4.1*), η_{ht} (*Section* 3), $C_{L_{\alpha_{ht}}}$ (*Section 4.1*), $\frac{\partial \varepsilon}{\partial \alpha}$ (*Section 5*), ε_0(*Section 5*) and ε_f (*Section 5.2*).

$$C_{L_{lon}} = C_{L_{0_{wb}}} + C_{L_{\alpha_{wb}}}\alpha + \mathrm{q}^* C_{L_q} + C_T C_{L_{CT}} + \eta_{ht}\frac{S_{ht}}{S}\left[C_{L_{\alpha_{ht}}}\left(\alpha - \alpha\frac{\partial \varepsilon}{\partial \alpha} + \delta_e - \varepsilon_0 - \varepsilon_f\right) + \delta_{e,TR} C_{L_{ht,\delta_{e,TR}}}\right] \quad \textbf{(5.12)}$$

$$C_{m_{lon}} = C_{m_{0_{wb}}} + C_{m_{\alpha_{wb}}}\alpha - \eta_{ht}\frac{l_t S_{ht}}{\bar{c}\, S}\left[C_{L_{\alpha_{ht}}}(\alpha - \alpha\frac{\partial \varepsilon}{\partial \alpha} + \delta_e - \varepsilon_0 - \varepsilon_f) + \delta_{e,TR} C_{L_{ht,\delta_{e,TR}}}\right] + q * C_{m_q} + C_T C_{m_{C_T}} \quad \textbf{(5.13)}$$

6. GROUND EFFECT MODELLING

Modelling aircraft motion during take-off and landing is challenging due to ground effect. This thesis defines equations for aerodynamic coefficients near the ground, focusing on wing geometry and height above ground. While based on simplified conditions and very limited data, this ground effect model offers useful insights into aircraft dynamics during these phases.

6.1. Ground effect influence on lift coefficient

As an aircraft nears the ground, its aerodynamic characteristics change significantly due to the influence of ground effect. The aircraft lift coefficient typically increases because of the air-cushion effect. At the same time, the downwash angle at the tailplane decreases as the ground limits the downward airflow, changing the lift coefficient of the tail.

The lift coefficient near the ground (Eq. 6.1-6.7) can be expressed as the sum of the free-air lift coefficient C_{LF} and the lift increment caused by the ground effect ΔC_{LGE}. This increment is dependent on parameters such as the wing's height above the ground h_w, the aspect ratio A, and the aircraft's lift curve slope a, the mean aerodynamic chord c and increment of wing-body pitching moment coefficient ΔC_{m0F} [36].

$$C_L = \left(1 + \frac{\Delta C_{L_{GE}}}{C_{LF}}\right) C_{LF} \tag{6.1}$$

$$\frac{\Delta C_{L_{GE}}}{C_{LF}} = \frac{1}{1 - \frac{a\sigma}{\pi A}} \{\frac{a\sigma}{\pi A} + \gamma[\frac{N}{(1 - \frac{\tau N C_{LF}}{1 - \frac{a\sigma}{\pi A}})^2} - 1]\} \tag{6.2}$$

$$\sigma = \exp\left[-2.48(\frac{2h_w}{b})^{0.768}\right] \tag{6.3}$$

$$\gamma = \sqrt{1 + (\frac{2h_w}{b})^2} - \frac{2h_w}{b} \tag{6.4}$$

$$\tau = \frac{\frac{h_w}{c}}{8\pi[(\frac{h_w}{c})^2 + \frac{1}{64}]} \tag{6.5}$$

$$N' = 1 + 0.00239[10\frac{c}{h_w} + 16\left(\frac{c}{h_w}\right)^2 + (\frac{c}{h_w})^3] \tag{6.6}$$

$$N = 1 + (\mathrm{N}' - 1)[1 + \frac{2\Delta C_{m0F}}{C_{LF}}] \tag{6.7}$$

6.2. Pitching moment adjustments due to ground effect

Ground effect also impacts the pitching moment of the aircraft. As the downwash angle at the tailplane decreases, there is an increase in the pitch-down moment. This change in downwash angle for a given angle of attack can be calculated using equations that account for the interaction between the wing and the ground.

The increment in the downwash angle due to ground effect $\Delta\varepsilon$ is influenced by several factors, the height of the tailplane's aerodynamic centre above the ground h_{ht}, the downwash angle at the tailplane in free air for a given angle of attack (Eq. 6.8) [36].

$$\Delta\varepsilon = -\varepsilon_f \frac{b^2{}_{eff} + 4(h_{ht} - h_w)^2}{b^2{}_{eff} + 4(h_{ht} + h_w)^2} \tag{6.8}$$

The effective span of the wing b_{eff}, combined with the wing's taper ratio λ and the span of the flaps, also contributes to the downwash increment (Eq. 6.9-6.11). These parameters influence how lift is distributed across the wing and tail, especially when flaps are deployed. The extension of the flaps causes a notable lift increment by altering the aerodynamic flow over the wing, which subsequently affects the tailplane [36].

$$\frac{b_{eff}}{b} = \frac{k_1 k_2 C_{LF}}{C_{LF} - (1 - k_2)(C_{LF} - \Delta C_{Lf}}) \tag{6.9}$$

$$k_1 = 0.085(7.56 + 3.5\lambda - \lambda^2) + 0.002(\lambda - 0.48)(A - 6)(18.5 - A) \tag{6.10}$$

$$k_2 = \sqrt{0.64 + 3.6\frac{b_F}{b} - (\frac{b_F}{b})^2} - 0.8 \tag{6.11}$$

The overall effect can be calculated using the distance l_t, which is the lever arm between the aerodynamic centre points of the wing and the tailplane.

Additionally, the wing and tailplane areas, S_w and S_{ht} respectively, are critical parameters in determining the overall pitching moment increment. The height of the wing's aerodynamic centre h_w and the height of the tailplane's aerodynamic centre h_{ht} above the ground are also factored into these calculations. These heights depend on the aircraft's geometry and the current state variables, which include parameters such as angle of attack and ground proximity.

From there, the increment of the lift coefficient of the tail can be calculated according to equations (6.12) and (6.13) [36].

$$\Delta C_{L_{ht_{GE}}} = -a_T[-\Delta\varepsilon + \frac{\beta\left(C_{L_{ht}} - a_{ht}\Delta\varepsilon\right)}{\pi A_{ht}}] \tag{6.12}$$

$$\beta = 0.00087[46\frac{b_{ht}}{h_{ht}} + 16.4\left(\frac{b_{ht}}{h_{ht}}\right)^2 - \left(\frac{b_{ht}}{h_{ht}}\right)^3] \quad \textbf{(6.13)}$$

Since the pitching moment is the result of the lifting force and the appropriate lever arm, the increment of the pitching moment due to ground effect can be expressed by equations (6.14) and (6.15) [36].

$$\Delta C_{m_{GE}} = -\overline{V}_H \Delta C_{L_{htGE}} \quad \textbf{(6.14)}$$

$$\overline{V}_H = \frac{l_{ht} S_{ht}}{c S_w} \quad \textbf{(6.15)}$$

6.3. Change in drag in ground effect

For drag, the total drag coefficient near the ground is the sum of the free air drag coefficient and an increment caused by the ground effect (Eq. 6.16-6.18). The reduction in induced drag near the ground plays a significant role in lowering the overall drag coefficient [36].

$$C_D = C_{DF} + \Delta C_{D_{GE}} \quad \textbf{(6.16)}$$

$$\Delta C_{D_{GE}} = \frac{\phi C_L}{\pi A} C_{DF} - [\sigma - (2 - \sigma)\frac{\phi C_L}{\pi A}] C_{DiF} \quad \textbf{(6.17)}$$

$$\phi = 0.00066[570\frac{b}{h_w} - 32(\frac{b}{h_w})^2 + (\frac{b}{h_w})^3] \quad \textbf{(6.18)}$$

This thesis incorporates the theoretical framework for the effects of ground proximity on drag; however, this aspect was excluded from the model. The decision was made because the parameters used in the model were estimated differently, and their validation against experimental or flight test data was beyond the scope of this work. Future research should focus on refining these parameters and integrating them into a comprehensive ground effect drag model.

7. IMPLEMENTATION IN SIMULATION AND RESULTS

7.1. Simulation setup in MATLAB/Simulink

7.1.1. Increments due to deployed flaps

The *iniac.m* MATLAB script serves as the foundation for the aircraft simulation, containing all the parameters needed to model the aircraft's performance and behaviour. It includes inputs for a variety of variables, such as aerodynamic coefficients, geometric properties, propulsion characteristics, landing gear configuration, and environmental conditions like atmospheric properties, etc.

As part of this work, the script was updated to incorporate new flap increments for the lift coefficient *CL_df (Section 4.2.1)*, drag coefficient *CD_df (Section 4.2.2)*, and pitching moment coefficient *Cm_df (Section 4.2.3)*. These values were recalculated using the ESDU methods described in previous chapters, replacing the existing values. By directly integrating these refined increments into the script, the simulation now reflects a higher level of accuracy and reliability regarding the aerodynamic effects of flap deflections.

The parameters were additionally manually tuned to ensure that the updated aerodynamic characteristics are seamlessly incorporated into the overall simulation.

7.1.2. Integration of downwash model in longitudinal dynamics model

In the Simulink model *model_aero.slx*, tail angle of attack and dynamic pressure blocks (*Figure 25* and *Figure 26*) were added to the lift coefficient and pitching moment coefficient blocks to improve the accuracy of the aerodynamic simulation. These additions account for the effects of downwash on the tail, which influences the lift generated by the tailplane and, in turn, the pitching moment. The dynamic pressure block ensures that the effect of the variations in pressure in the wake, and its effect on the tail lift coefficient, is modelled for changing angles of attack.

Additionally, the wing-body and tail influences were separated.

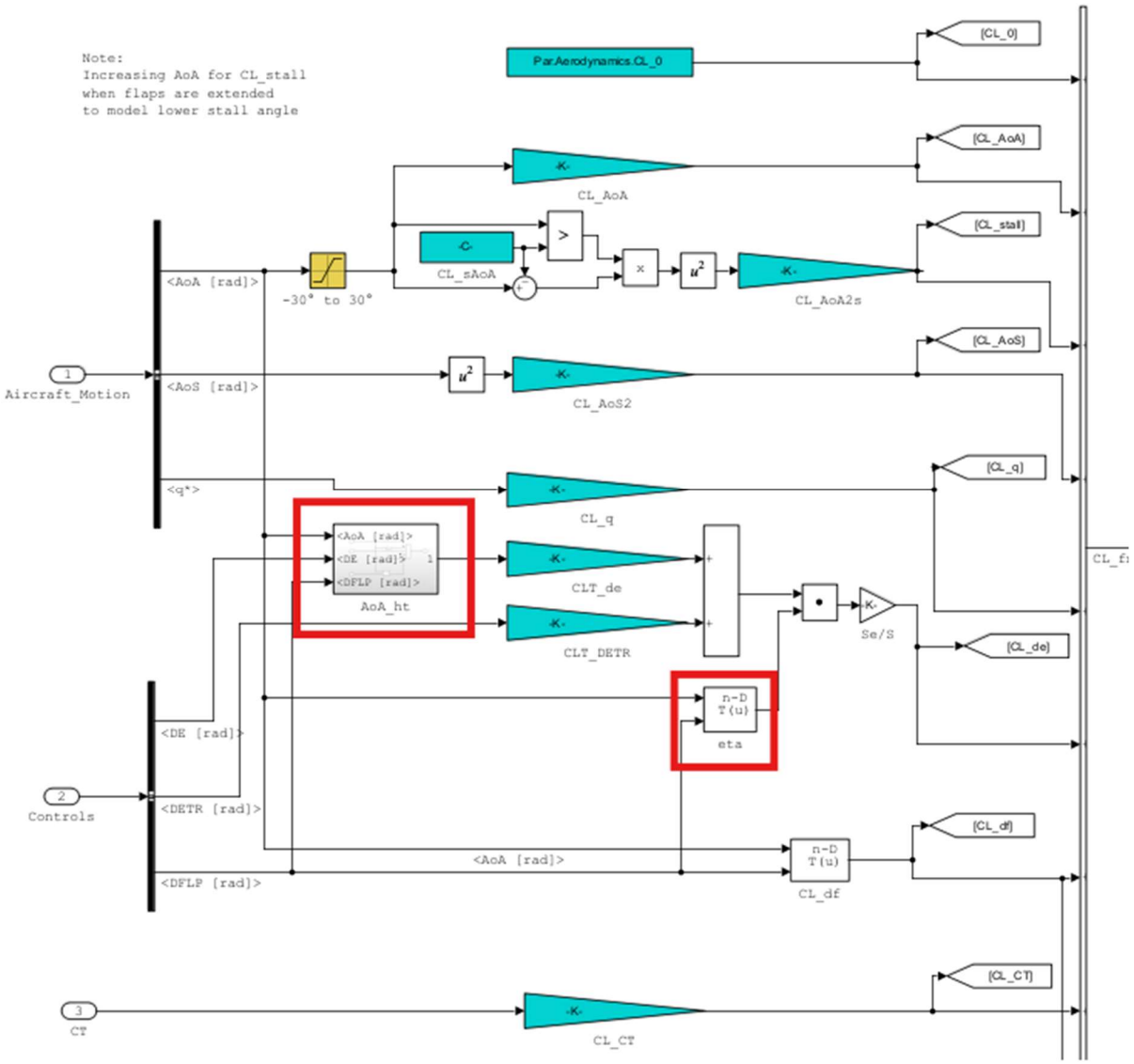

Figure 25 Lift coefficient Simulink model

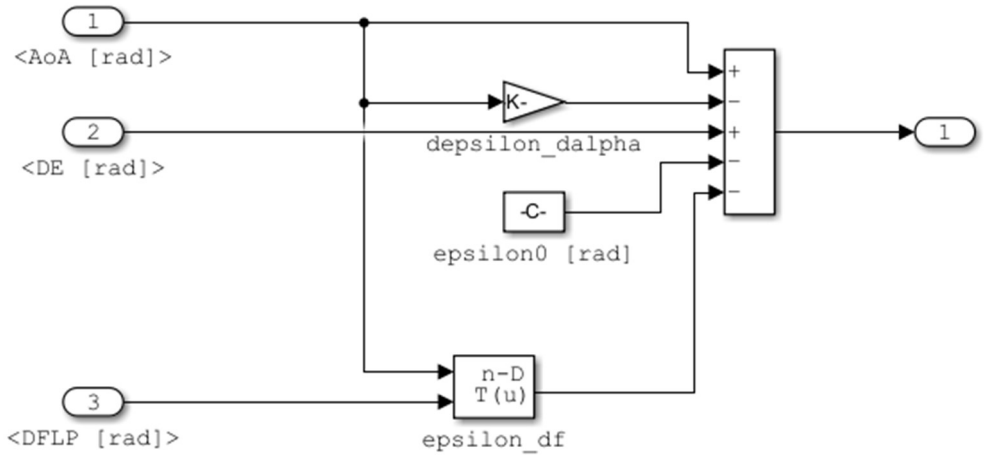

Figure 26 Stabilator angle of attack Simulink block

The parameters required for these blocks, such as downwash gradient *depsilon_dalpha (Section 5.1)*, downwash angle increment for deployed flaps *epsilon_df* (*Section* 5.2) and dynamic pressure values *eta_df (Section 5.3)*, are defined in the *iniac.m* script, ensuring consistency across the simulation. This integration provides a more realistic representation of the interactions between the main wing and tail aerodynamic characteristics.

7.1.3. Integration of ground effect model

In the *model_aero.slx* Simulink model, new blocks for ground effect were added. These blocks, implemented as MATLAB function blocks, calculate the increments in lift *(Section 6.1)* and pitching moment *(Section 6.2)* due to ground proximity, using the aerodynamic coefficients in free stream conditions. The existing blocks from the previous ground effect model were removed, as the new model follows a different approach and is not compatible with the old one. No additional parameters were added to the *iniac.m* script, as the new calculations utilize the aerodynamic data already defined within the simulation.

7.2. Results

7.2.1. Longitudinal aerodynamic model

Figure 27 shows the overall longitudinal aerodynamic coefficients of the aircraft during a glide. The parameters used for this analysis include a thrust coefficient C_T of 0.02 and an elevator deflection δ_e of -6°. The results are shown for the aircraft in a clean configuration as well as with flaps deployed at angles of 10°, 25°, and 40°. This comparison highlights the effects of different flap settings on the aerodynamic behavior of the aircraft during gliding flight.

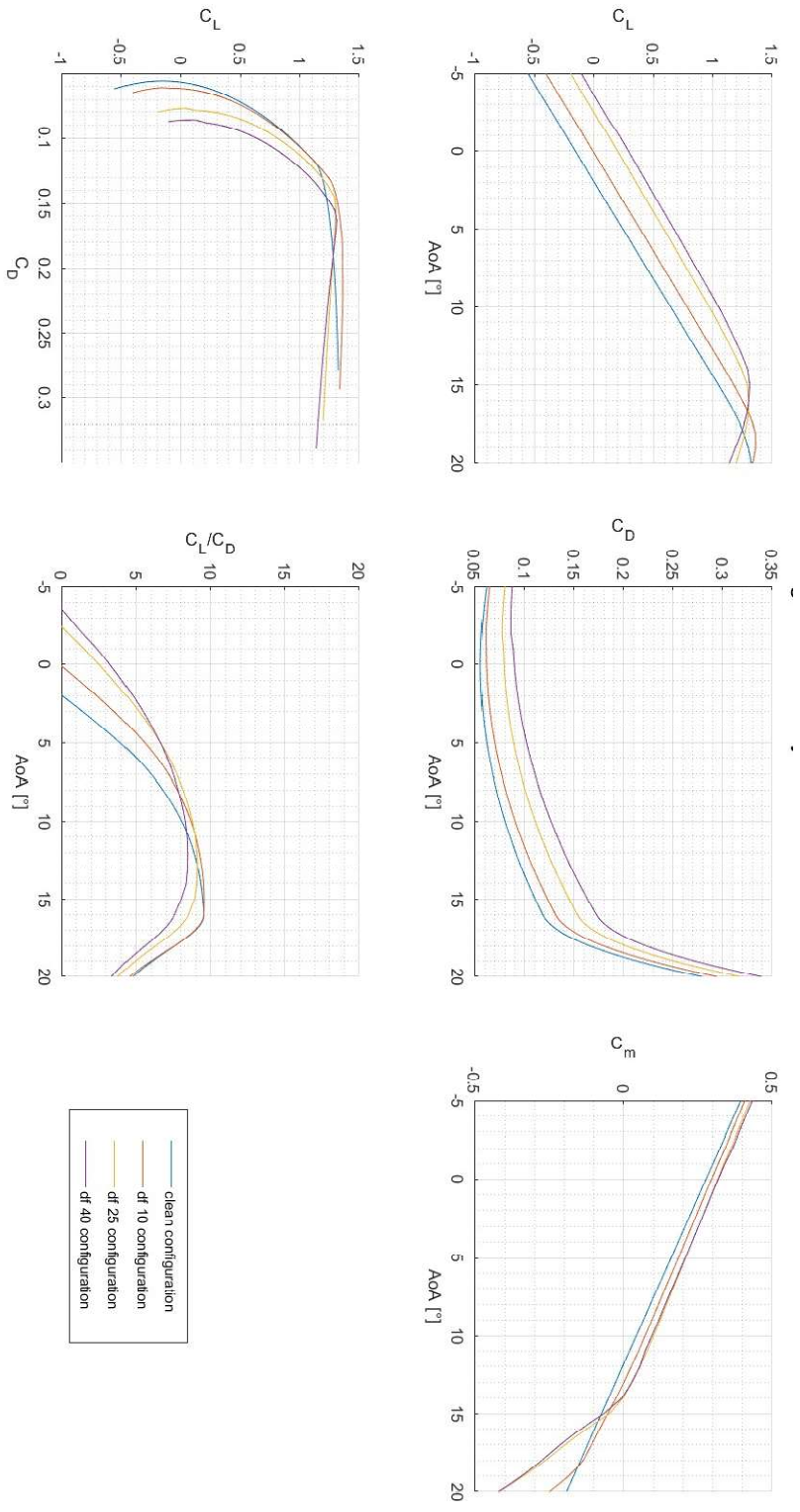

Figure 27 PA-28 Overall aircraft longitudinal aerodynamic coefficients at a glide

7.2.2. Comparison of the longitudinal aerodynamic parameters

Figure 28,*Figure **29*** and*Figure **30*** show a comparison of the lift, drag, and pitching moment coefficients between the new model S_N and the old PA-28 model S_O under identical conditions. The parameters for this analysis again include a thrust coefficient C_T of 0.02 and an elevator deflection δ_e of -6°. In the following plots, the dashed lines represent the old model, while the solid lines correspond to the new model. This comparison highlights the differences in aerodynamic performance between the two models under the same specified flight conditions, with a varied angle of attack.

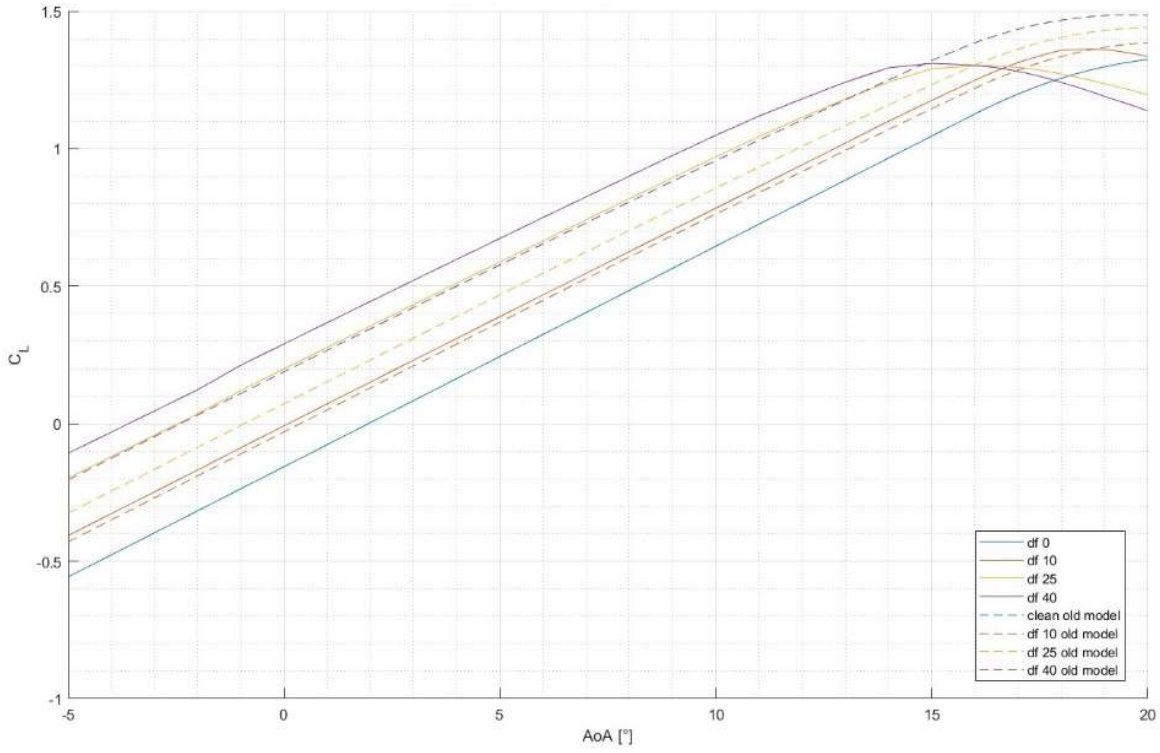

Figure 28 Lift coefficient results comparison - new and old model

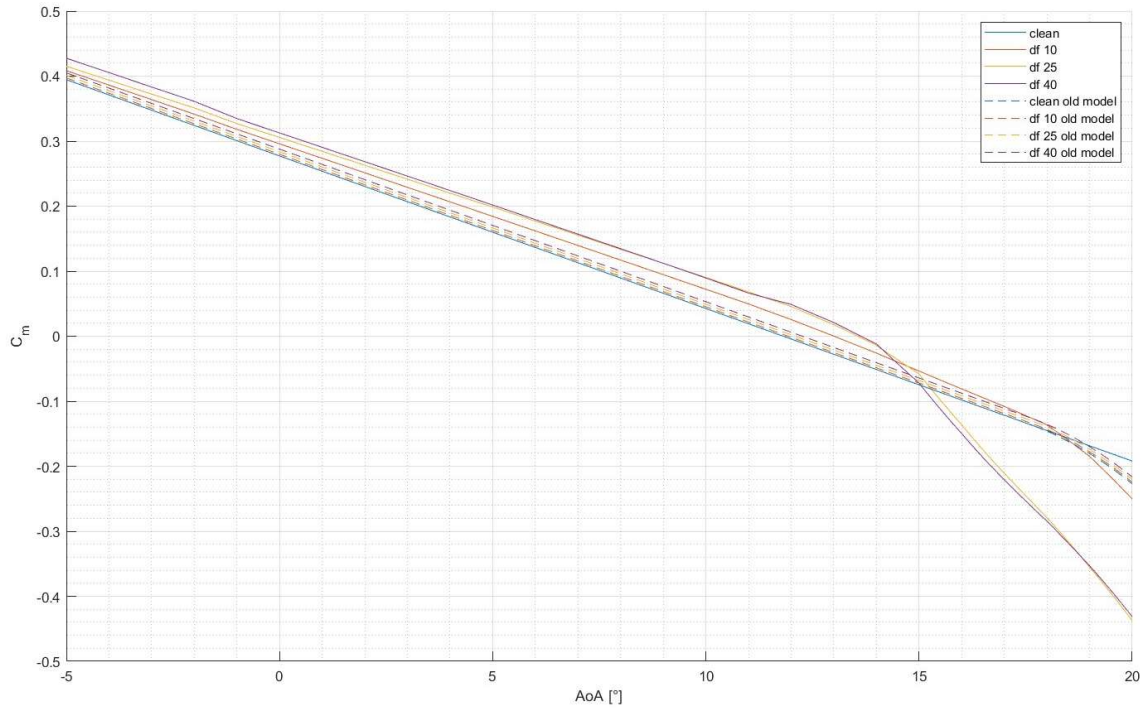

Figure 29 Pitching moment coefficient results comparison - new and old model

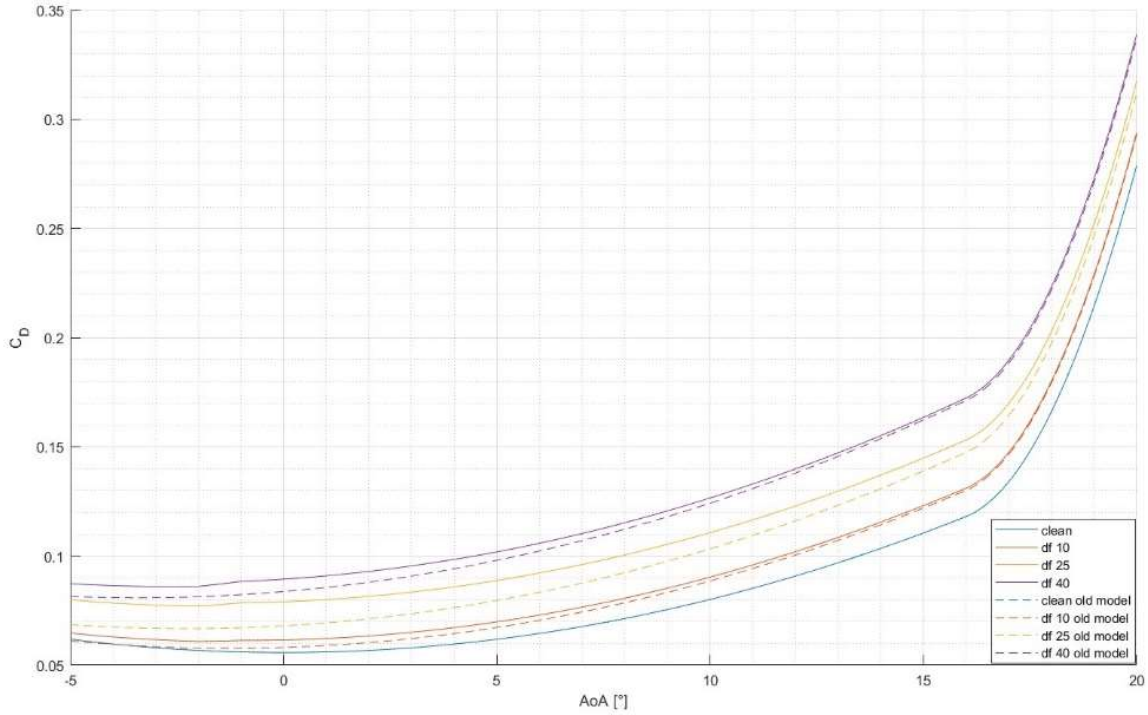

Figure 30 Drag coefficient results comparison - new and old model

7.2.3. Tests on the simulator

This chapter presents the results of tests conducted using the ReDSim (Research and Didactics Simulator) at the ZHAW. The ReDSim is a real-time research and teaching simulator, developed by the Center for Aviation in collaboration with students and staff. It incorporates advanced technology, including a Control Loading System for realistic force feedback and a 180-degree visual system, providing an immersive and accurate simulation environment [37].

Figure 31 ReDSim at the ZHAW

Two tests were conducted to evaluate the updated PA-28 model: a trim test and landing test. The trim test was performed by one pilot, focusing on steady-state flight conditions, while the landing tests were carried out by another pilot across various flap configurations. Both pilots hold a current license and have experience flying the Piper PA-28-161 Warrior III, ensuring qualified and informed feedback. Their insights on the model's performance and realism are summarized alongside the simulation results in this chapter.

7.2.3.1 Trim test

To further compare the models, a trim test was conducted to evaluate their behaviour under various configurations. The test involved initiating a steady flight and trimming the aircraft in a clean configuration. Following this, flaps were incrementally deflected to 10°, 25°, and 40°, with the aircraft trimmed after each deflection. This process was repeated for each flap setting to assess the performance of both models and analyse their responses to changes in flap configuration.

Table 4 compares results of the trim test for clean configuration and flap deflections at 10°, 25°, and 40°. It shows the differences in pitch angle between the two models, for a similar angle of attack.

Table 4 Trim test performance results – Simulation old model (S_O), Simulation new model (S_N)

δ_f [°]	θ [°]		α [°]	
	S_O	S_N	S_O	S_N
0	6.5	7.1	6.6	6.7
10	5.6	6.6	5.0	5.2
25	4.1	4.7	4.0	4.1
40	3.2	3.5	3.3	3.3

The results of this test are presented in *Figure 32* and*Figure **33***.

During the trim test, pilot Tobias Zihlmann noted that in the old model, the pitch-up motion with flaps deployed at 40° was less realistic compared to the behaviour of the real aircraft. In contrast, the updated model exhibited a response more closely resembling the actual PA-28.

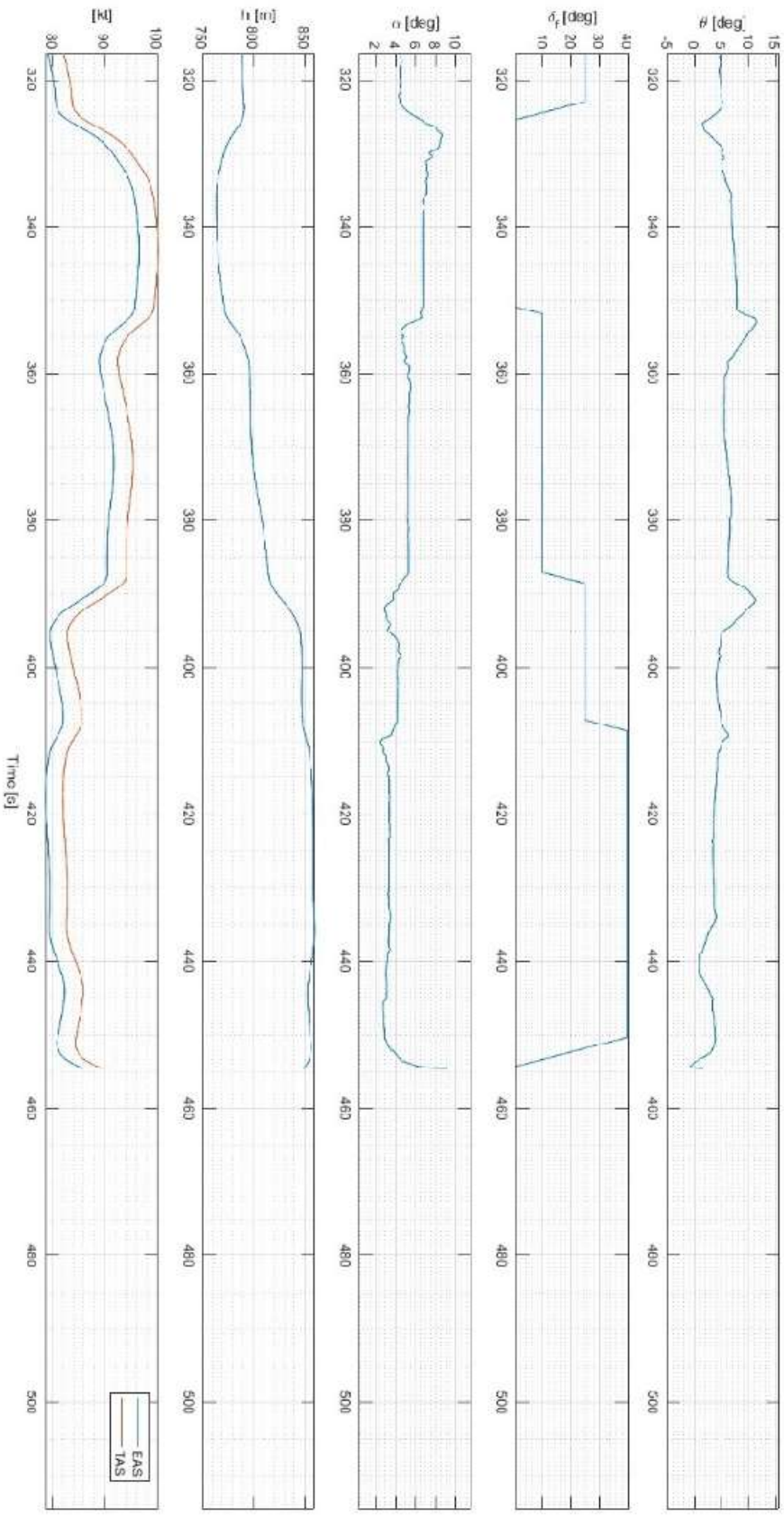

Figure 32 Trim test new model

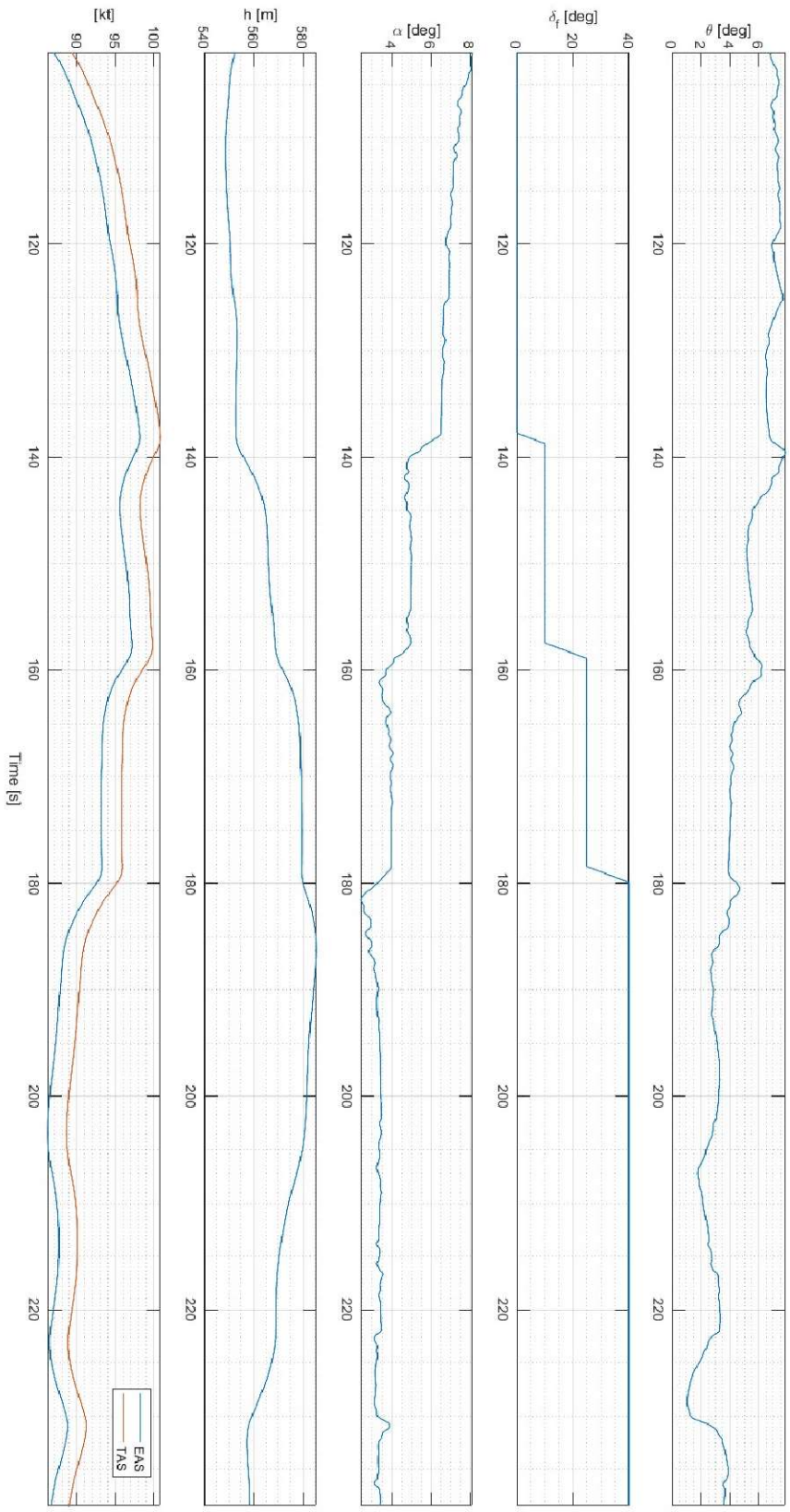

Figure 33 Trim test old model

7.2.3.2 Ground Effect

Ground effect data was collected from three landings done during the flight test campaigns. These tests were performed in three configurations: clean configuration, flaps at 25°, and flaps at 40°. The same landing scenarios were then simulated with Pedrazzini's model and with the new model to evaluate their performance in comparison to the original data. In order to effectively measure the performance of the new model, results from Pedrazzini's model were recreated to be used as a reference.

Table 5 shows the parameters for the landing scenarios from the flight test FT, the old simulation model S_O, and the new simulation model S_N. The table includes estimated values for airspeed, RPM, pitch angle, and elevator deflection, allowing a clear comparison between the models and the flight test results.

Table 5 Final approach performance results – Fligh test (FT), simulation old model (S_O), Simulation new model (S_N)

δ_f [°]	EAS [kt]			RPM			θ [°]			δ_e [°]		
	FT	S_O	S_N	FT	S_O	S_N	FT	S_O	S_N	FT	S_O	S_N
0	73	74	73	1500	1500	1500	7	7.5	7.5	-6.5	-7	-7
25	70	70	70	1400	1400	1400	4	4.9	3.5	-5	-5.9	-3
40	67	67	67	1400	1400	1400	3	4.0	3	-4.5	-5.8	-3.5

Figure 34 and*Figure **35*** display the longitudinal motion parameters and ground effect parameters for landings simulated using the old model. *Figure 36* and*Figure **37*** provide a detailed comparison of the lift and pitching moment increments in the clean configuration for both the old and new models. Finally, *Figure 38* and*Figure **39*** present the longitudinal motion parameters and ground effect parameters for landings with flaps deployed, as simulated using the new model.

For the landing tests, pilot Marco Caglioti observed that the updated model had better stability during approach and landing. He also mentioned that the flap behaviour in the old model was not very accurate, whereas the new model provided a more realistic representation of the aircraft's performance with flaps deployed.

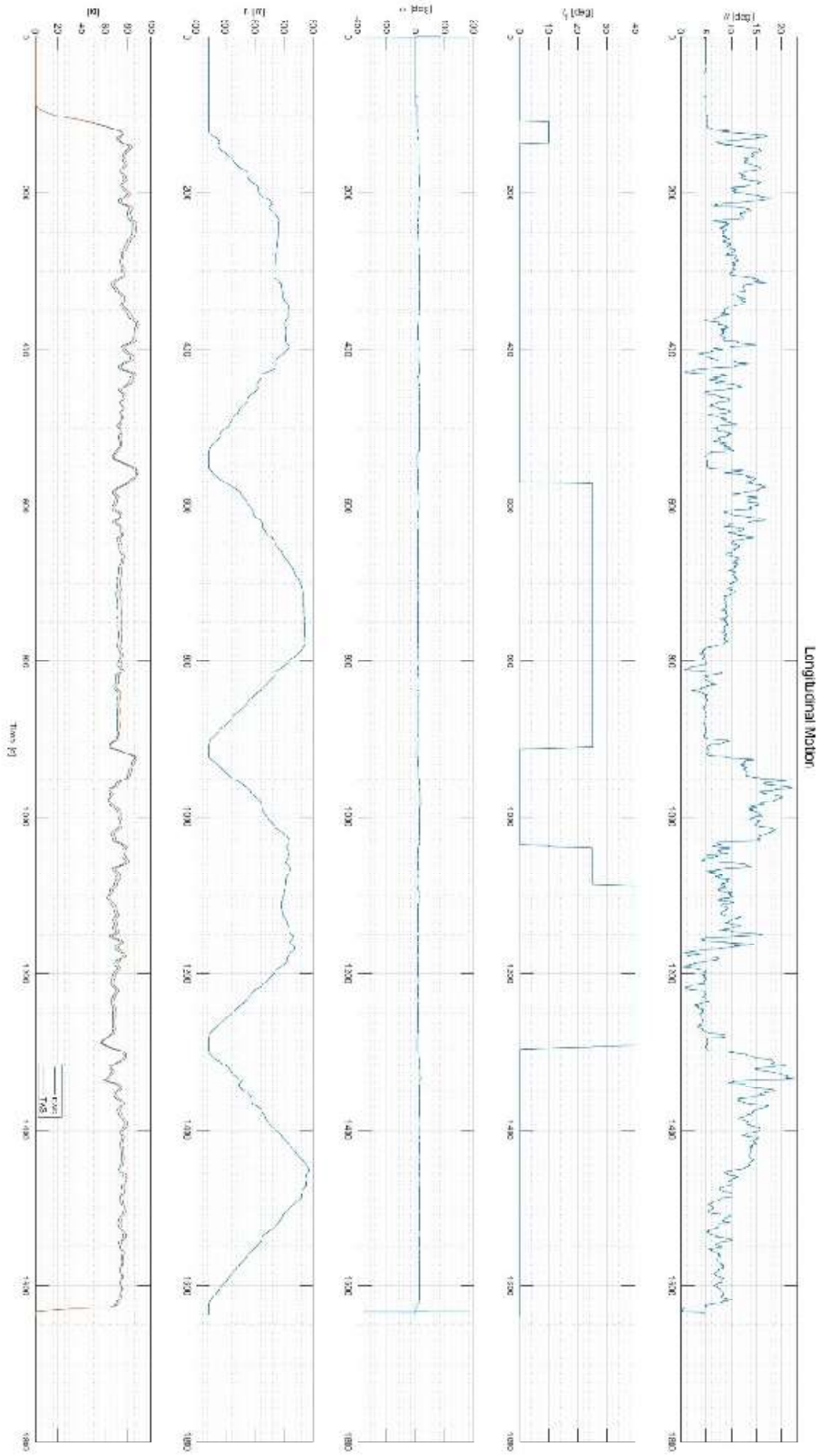

Figure 34 Final approach longitudinal motion parameters in clean configuration and configuration with flaps deplayed at 25° and 40° S_O

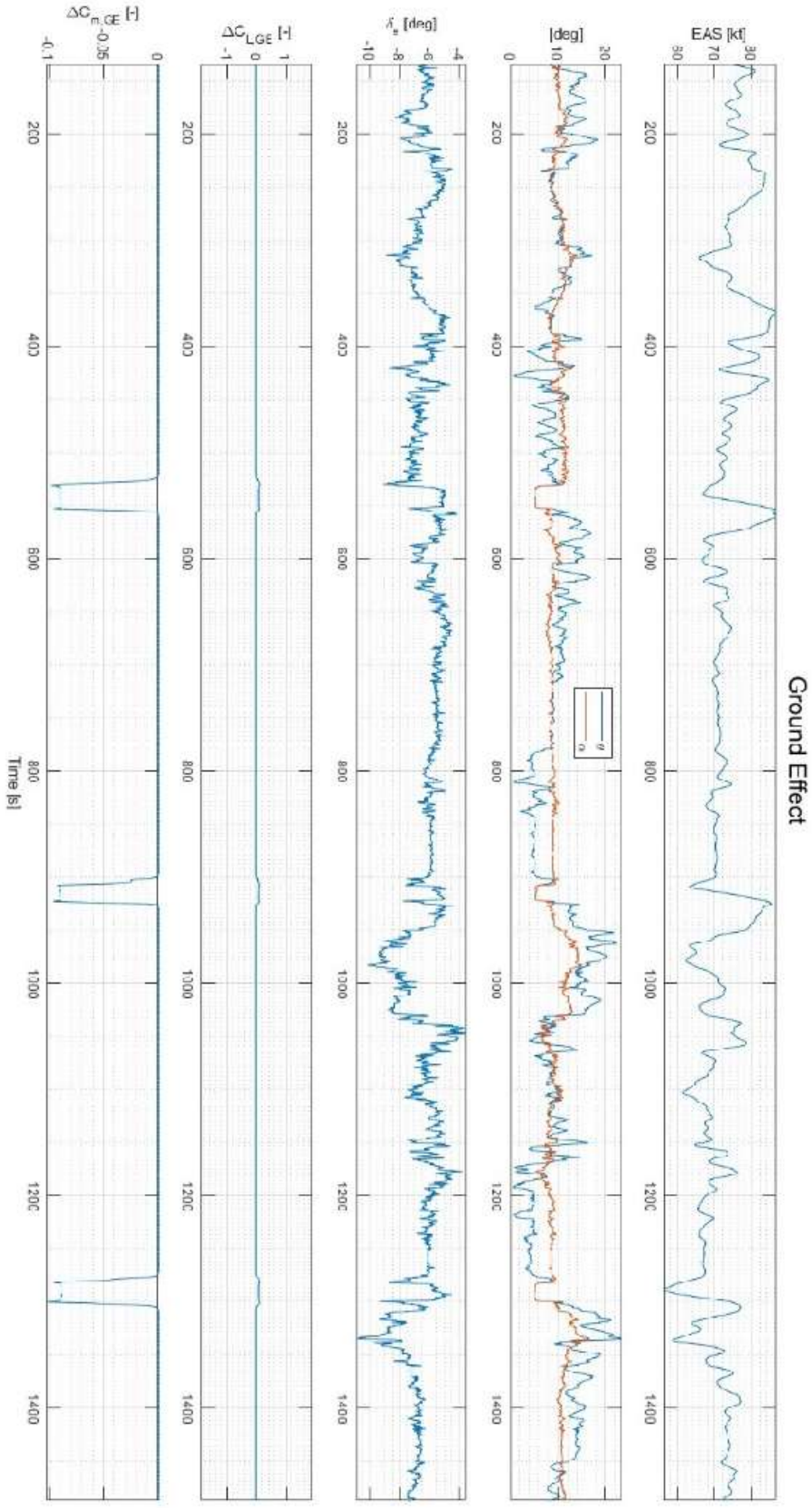

Figure 35 Ground effect parameters for final approach in clean configuration and configuration with flaps deplayed at 25° and 40° S_O

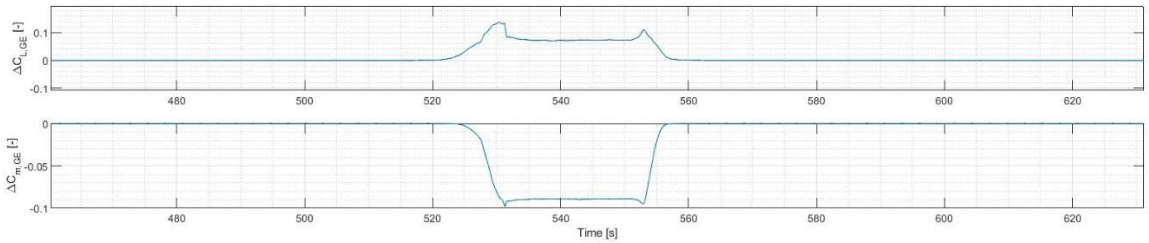

Figure 36 Ground effect parameters for final approach in clean configuration S_O

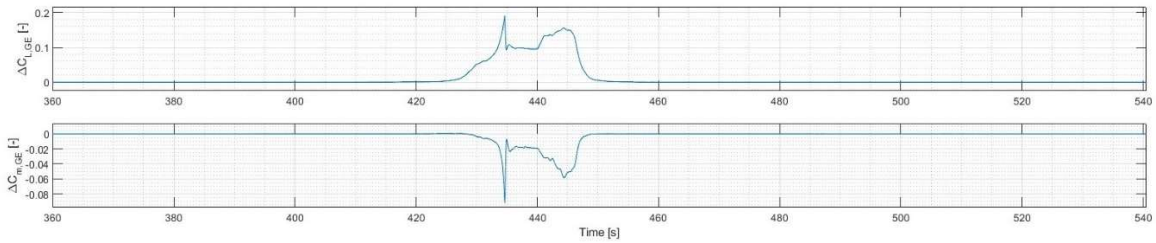

Figure 37 Ground effect parameters for final approach in clean configuration S_N

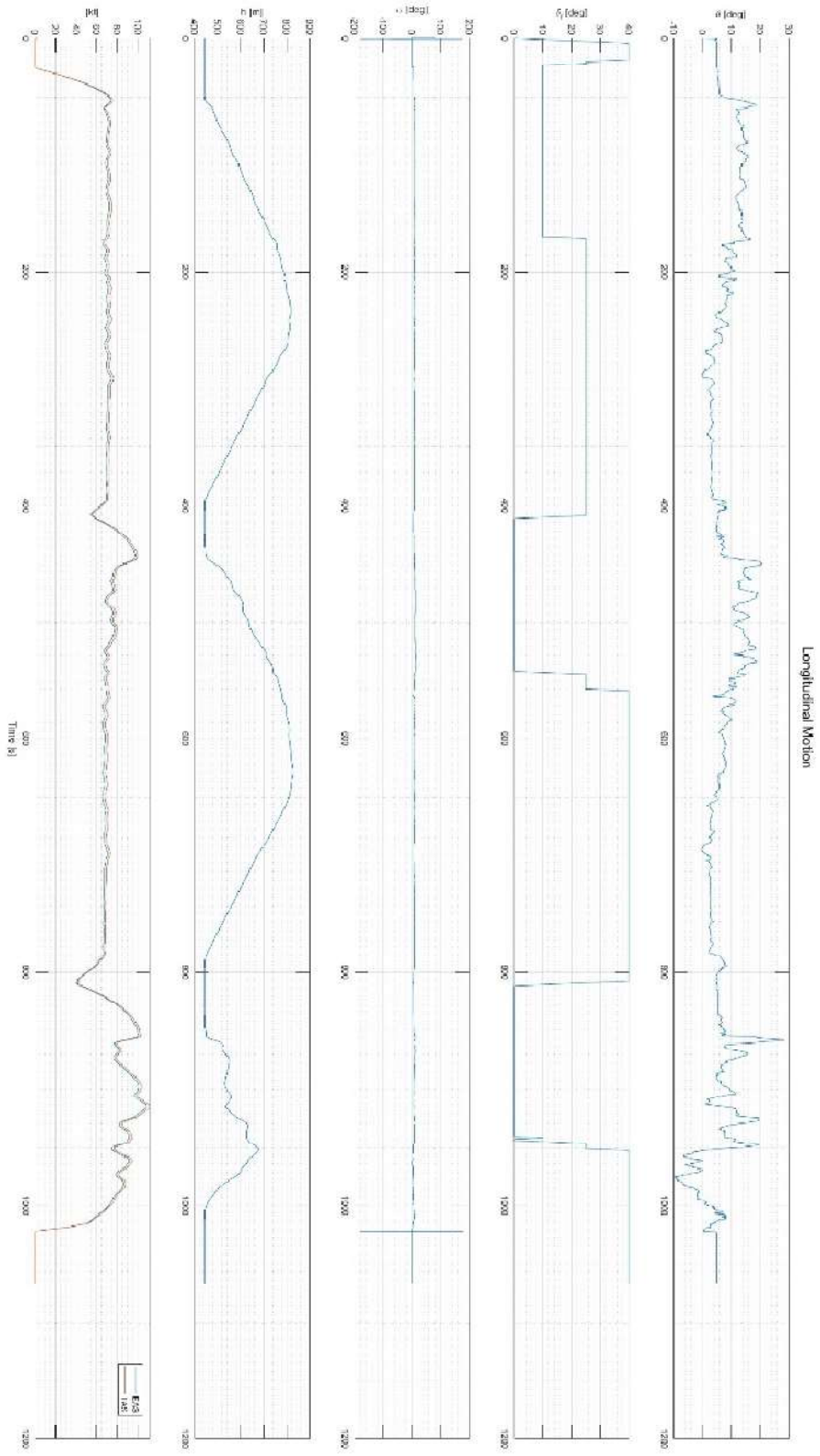

Figure 38 Final approach longitudinal motion parameters in configuration with flaps deplayed at 25° and 40° S_N

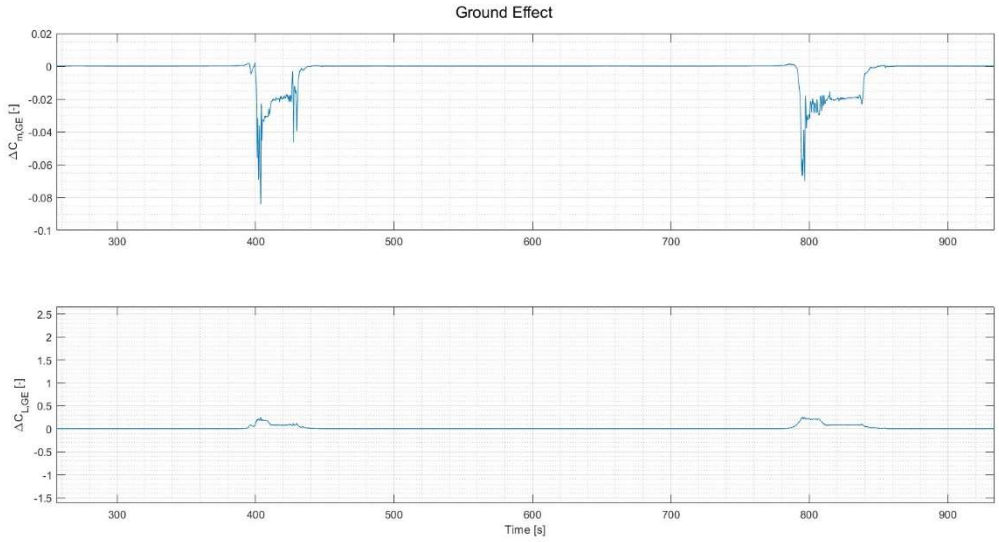

Figure 39 Ground effect lift and pitching moment coefficient increments for final approach in configuration with flaps deplayed at 25° and 40° S_O

8. DISCUSSION

8.1. Comparative analysis: new vs. old model

8.1.1. Lift

The most significant modifications in the new lift model are due to the flaps model, which is evident from the differences in the lift coefficient curves. In contrast, the downwash and ground effect contributions are less noticeable.

A noticeable lift increment can be observed (*Figure 27*) when the flaps are deployed, with a relatively similar increase between the 10° and 25° flap configurations. However, the lift increment for the 40° flap setting is smaller, which aligns with expectations based on the flap model described in Section 4.2. The maximum lift values correspond well with the respective flap settings, indicating accurate representation of the increased lift potential for each configuration.

Additionally, the angle of attack for maximum lift was manually adjusted to account for the effects of the aircraft's body and tail, which influence the flow and alter the expected angle of attack for maximum lift.

Comparison with Pedrazzini's model (*Figure 28*) shows that the lift increment is no longer consistent across all flap deflections and that the maximum lift coefficient differs significantly in both value and angle of attack for achieving maximum lift. Pedrazzini's model [2] uses a simpler approach where the clean configuration serves as the baseline, with the same gain increment added for both the linear and non-linear parts of the lift curve. This highlights the improved realism of the new model in capturing variations in lift behaviour across different flap settings.

8.1.2. Pitching moment

The pitching moment coefficient across angles of attack for the overall aircraft shows that the aircraft remains aerodynamically stable despite the inherent instability of the wing. The stability of the aircraft is achieved by the contribution of the tailplane, which counteracts the aerodynamic instability of the wing.

The flap model is based on the wing's behaviour, as described in Section 4.2. Flap deflections at 10° and 25° result in a more significant increase in C_m compared to 40°, as expected.

The effect of downwash is particularly evident in *Figure 27* and *Figure 29*. Downwash alters the lift force and the angle of attack at the tailplane, which in turn impacts the pitching moment. This effect becomes more pronounced with flap deflection, as pitching moment increment and downwash angle contribution from the wing interact more strongly with the tailplane, affecting its aerodynamic contribution.

The stall region should be highlighted, especially when comparing the results with Pedrazzini's model (*Figure 29*). In the new model, the pitching moment for flaps set at 25° and 40° rapidly declines in the stall region because it is directly based on the lift generated by the wing. As lift decreases sharply during stall, the pitching moment reduces accordingly, reflecting the critical influence of lift on the model's behaviour in this area.

While Pedrazzini's model offers a simpler representation, it is not reliable for modelling stall behaviour. However, as modelling stall was beyond the scope of this thesis, the stall region is included in this model to ensure the simulator model behaves smoothly, emphasizing the limitations of the ESDU method described in Section 4.2.3 and of Pedrazzini's approach [2].

8.1.3. Drag

As expected, the drag coefficient increases with angle of attack for all configurations, with a more pronounced rise at higher angles of attack due to increased induced drag. Additionally, the deployment of flaps significantly increases the drag coefficient, as flaps add both form drag and lift-induced drag. The increment is larger for higher flap deflections, with flaps at 40° producing the most drag which aligns with the ESDU method results (Section 4.2.2).

When comparing the new model to the old model (*Figure 30*), the new model predicts slightly higher drag coefficients for all configurations, but especially for configuration with flaps deployed at 25°. This discrepancy becomes more pronounced at lower angles of attack. This suggests improved modelling of form drag compared to the old model, which is due to the more accurate single-slotted flap model.

8.1.4. Trim test

The trim test results, summarized in *Table 4*, provide a comparison of the old simulation model and the new simulation model for different flaps configurations.

The test compares the pitch angle and angle of attack for the trim conditions in both models across the flap configurations. The results show a slight increase in pitch in the new model

compared to the old model for a similar angle of attack. This difference is attributed to the implementation of a new downwash model and the correction of the pitching moment increment due to flap deflections in the new model. The addition of the downwash reduces the angle of attack at the tailplane, which lowers the lift force generated by the tail. This reduction in tail lift causes the nose-up rotation in the new model.

8.1.5. Ground effect

Three landing tests were simulated with the updated model to compare its performance against flight test results and the original model. *Table 5* summarizes the landing scenarios, including estimated airspeed, RPM, pitch angle, and elevator deflection.

The new model's pitch angle closely matches the flight test data, showing it accurately represents the aircraft's trim and stability. However, there are small errors in elevator deflection. In the old model, the elevator deflection was more negative than in the flight test, while the new model shows slightly more positive deflection. This difference likely comes from the updated flap pitching moment increment in the new model, which reduces the force needed from the tailplane. As a result, the required elevator deflection is less negative.

These elevator deflection errors are partly due to how the parameters were tuned. The tuning process focused on the pitching moment increment, with less emphasis on fine-tuning the downwash model. Additionally, a slight increase in pitch noted during trim testing (Section 8.1.4) affects the results. For the same angle of attack and elevator deflection, the pitch angle in the new model is slightly higher. Aligning the pitch angle with flight test data introduces small errors in angle of attack and elevator deflection.

The differences in ground effect increments are most noticeable in the clean configuration, where the flap increments don't play a role. In this case, the ground effect and downwash models are the main contributors to the results.

The analysis shows that the new model predicts a larger lift increment and a smaller pitching moment increment compared to the old model. This is due to ground effect increasing lift and reducing downwash at the tailplane, which lowers pitching moment values. Similar patterns are seen in landings with flaps set at 25° and 40°.

8.2. Limitations of the current model

The current simulation model has some limitations that affect its accuracy. These come from both the characteristics of Pedrazzini's model and the goals and limits of this thesis, including time constraints. While improvements were made, there are areas that need more work to make the model more reliable and effective.

Thrust model

The thrust parameters used in this study are taken from Pedrazzini's model, which he noted as unreliable in his work. These parameters were not updated, so better modelling of thrust performance and its effect on longitudinal and lateral aerodynamics is still needed.

Overall aircraft drag coefficient

The drag model for the flaps was improved using ESDU methods. However, the overall drag of the aircraft still needs more work. For example, changes made to the lift model, like adding a downwash model, might affect induced drag predictions. This needs further study to make the drag estimates more accurate.

Stall model

The way stall is represented in the current model isn't very accurate. While updates were made to the flaps model, the stall behaviour itself needs more improvement. Smoother transitions were added to the simulation, but a better stall model is still required.

Downwash impact on stability and control

The effect of the downwash model on the aircraft's stability and control wasn't fully studied. Even though downwash was added to the simulation, its overall impact on stability needs more analysis.

Transition dynamics during configuration changes

The simulation mainly focused on steady flight conditions. It didn't model how the aircraft behaves dynamically when flaps are deployed or during similar transitions. These dynamic responses are important for a more complete simulation but were not included in this thesis.

Ground effect data

The ground effect model is limited because only three landings were used for analysis. More flight tests are needed, especially during the final approach phase, with detailed data collected for all flap settings.

Ground effect at boundaries conditions

Unusual peaks in lift and pitching moment coefficients were seen in the simulation when the aircraft was close to the ground (e.g., at the start of the approach). These were not fully investigated and could mean the ground effect model isn't accurate.

Elevator deflection errors

The pitch values in the simulation matched flight test data well, but there were small errors in elevator deflection. This is likely because the focus was on tuning the pitching moment model, which affected the accuracy of the downwash and ground effect models. More adjustments to the tailplane and downwash parameters are needed.

9. CONCLUSION

This thesis improved the PA-28 simulation model by focusing on three main areas: refining the flap model, developing and adding a new downwash model, and updating the ground effect model. These changes aimed to create a more accurate representation of the aircraft's longitudinal aerodynamic behaviour.

The flap model was significantly improved. A new model for the single-slotted flaps was developed using ESDU methods to capture both linear and non-linear aerodynamic effects. This updated model predicts lift, drag, and pitching moment coefficients more accurately for flap settings of 10°, 25°, and 40°.

A new downwash model was also integrated. This model accounts for how downwash affects the tailplane, including changes in lift and pitching moment caused by variations in the downwash angle. It calculates the downwash gradient, downwash angle, and dynamic pressure loss to better represent the interaction between the wing wake and the tailplane.

The ground effect model was improved as well. The updated model calculates how ground proximity affects lift, drag, and pitching moment coefficients, offering a more realistic view of the aerodynamic changes during landing and take-off. Despite limited flight test data, the model's results align well with flight test observations.

Future work should explore the downwash model further, especially its impact on stability and control during dynamic manoeuvres. Additional flight tests during final approach and across all flap settings would refine the ground effect model. More detailed modelling of stall behaviour and transitions, such as flap deployment, is also recommended. Finally, spending more time tuning the simulator parameters would address minor discrepancies in elevator deflection and pitching moment predictions. These steps would create a stronger and more accurate simulation model for various flight conditions.

REFERENCES

[1] Jackson, P., Munson, K., Peacock, L., *Jane's All the world's aircraft*, Janes Information Group; 98th edition, 2007-2008.

[2] Pedrazzini, N., "Piper PA-28 Simulation Model Development Based on Flight Test Data" Master's thesis, ZHAW School of Engineering, Winterthur, 2023.

[3] Haber-Zelanto, D., "Aerodynamic Coefficients Estimation of a General Aviation Airplane from Flight Test Data", Master's thesis, University of Zagreb, Zagreb, 2021.

[4] Đeverlija, J. J., "Aerodynamic Model Development for General Aviation Aircraft Based on Flight Test Data", Master's thesis, University of Zagreb, Zagreb, 2021.

[5] Spillmann, K., "Flight Testing of a General Aviation Aircraft and Simulation Model Development", Master's thesis, ZHAW School of Engineering, Winterthur, 2019.

[6] ESDU, https://www.esdu.com/cgi-bin/ps.pl?sess=unlicensed_1241107191913gkd&t=root&p=aboutusroot# (Date Accessed: 01.10.2024)

[7] NACA to NASA to now, https://www.nasa.gov/history/history-publications-and-resources/nasa-history-series/naca-to-nasa-to-now/ (Date accessed: 01.10.2024)

[8] About the STI Repository, https://sti.nasa.gov/what-is-the-sti-repository/ (Date accessed: 01.10.2024)

[9] Jategaonkar, R. V., *Flight Vehicle System Identification: A Time-Domain Methodology*, Second Edition. Reston (VA): American Institute of Aeronautics and Astronautics, Inc., 2015.

[10] ESDU, *Installed tailplane lift-curve slope at subsonic speeds*, ESDU 89029, Amendment (B), IHS Global Ltd., 2015.

[11] Piper Aircraft, Warrior III PA-28-161, *Pilot's Operating Handbook and FAA Approved Airplane Flight Manual*. BB-1565 FAA, Piper Aircraft Corporation, Publications Department, 1994.

[12] ESDU, *Lift curve of wings with high-lift devices deployed at low speeds*, ESDU 96003, Amendment (E), IHS Global Ltd., 11.2003.

[13] ESDU, *Introduction to the estimation of the lift coefficients at zero angle of attack and at maximum lift for aerofoils with high-lift devices at low speeds,* ESDU 94026, Amendment (A), IHS Global Ltd., 03.2000.

[14] ESDU, *Aerofoil maximum lift coefficient for Mach numbers up to 0.4,* ESDU 84026, Amendment (C), IHS Global Ltd., 03.2000.

[15] ESDU, *Wing lift coefficient increment at zero angle of attack due to deployment of plain trailing-edge flaps at low speeds*, ESDU 97011, Amendment (A), IHS Global Ltd., 01.2004.

[16] ESDU, *The maximum lift coefficient of plain wings at subsonic speeds,* ESDU 89034, Amendment (A), IHS Global Ltd., 03.2000.

[17] ESDU, *Wing angle of attack for zero lift at subcritical Mach numbers*, ESDU 87031, Amendment (C), IHS Global Ltd., 07.2013.

[18] ESDU, *Wing lift increment at zero angle of attack due to deployment of single-slotted flaps at low speeds,* ESDU 93019, Amendment (A), IHS Global Ltd., 03.2000.

[19] ESDU, *Maximum lift of wings with trailing-edge flaps at low speeds,* ESDU 91014, Amendment (A), IHS Global Ltd., 03.2000.

[20] ESDU, *Increment in wing profile drag coefficient due to the deployment of a single-slotted flap*, ESDU 08013, IHS Global Ltd., 03.2008.

[21] ESDU, *Aerofoil skin friction drag for Mach numbers below the drag-rise condition*, ESDU 06001, IHS Global Ltd., 02.2006.

[22] ESDU, *Aerofoil profile drag for Mach numbers below the drag rise condition*, ESDU 00027, Amendment (A), IHS Global Ltd., 02.2006.

[23] ESDU, *Profile drag coefficient increment due to full-span single-slotted flaps (Handley Page and NACA types)*, ESDU Aero F.02.01.06, Amendment (B), IHS Global Ltd., 04.2006.

[24] ESDU, *Vortex drag coefficient of wing with part-span flap and central cut-out*, ESDU Aero F.02.01.08, Amendment (E), IHS Global Ltd., 12.2013.

[25] ESDU, *Wing viscous drag coefficient in shock-free attached flow*, ESDU 07002, Amendment (A), IHS Global Ltd., 12.2011.

[26] ESDU, *Pitching moment curve of wings with leading-edge and trailing-edge high-lift devices deployed at low speeds*, ESDU 03017, Amendment (A), IHS Global Ltd., 04.2007.

[27] ESDU, *Aerodynamic characteristics of aerofoils in compressible inviscid airflow at subcritical Mach numbers*, ESDU 72024, Amendment (D), IHS Global Ltd., 03.2000.

[28] ESDU, *Aerofoil and wing pitching moment coefficient at zero angle of attack due to deployment of trailing-edge single-slotted flaps at low speeds*, ESDU 99004, Amendment (B), IHS Global Ltd., 01.2004.

[29] Deperrois, A., *Part IV Theoretical limitations and shortcomings of xflr5*, Rev. 1.0, 2019.

[30] Gudmundsson, S., *General Aviation Aircraft Design Applied Methods and Procedures*, Butterworth-Heinemann; 2nd edition, 2022.

[31] Etkin, B., Reid, L. D., *Dynamics of Flight: Stability and Control*, Wiley; 3rd edition, 1995.

[32] Yahyaoui, M., A New Method for the Prediction of the Downwash Angle Gradient, . International Journal of Aviation, Aeronautics, and Aerospace, Volume 6, Issue 3, 2019.

[33] Raymer, D. P., *Aircraft Design: A Conceptual Approach*, American Institute of Aeronautics and Astronautics, Inc. 5th edition, 2012

[34] ESDU, *Average downwash at the tailplane at low angles of attack and subsonic speeds*, ESDU 80020, Amendment (B), IHS Global Ltd., 02.2012.

[35] Silverstein, A., Katzoff, S., Design charts for predicting downwash angles and wake characteristics behind plain and flapped wings, NACA report No. 648, Langley Memorial Aeronautical Laboratory, U.S., Government Printing Office, 1939.

[36] Liu, H.H., *Dynamic characteristics of flight near the ground*, Civil Aviation Institute of China, American Institute of Aeronautics and Astronautics, Inc., 1987.

[37] ZHAW ReDSim, https://www.zhaw.ch/en/engineering/institutes-centres/zav/air-vehicle-design-and-technology/flight-mechanics-and-flight-control-systems/redsim-laboratory/, (Date Accessed: 02.12.2024)

Attachments

I. The complete Piper PA-28-161 Warrior III simulation model is attached to this thesis (PA28_vukovmag.zip)

II. XFLR5 Piper PA-28-161 Warrior model (XFLR5_vukovmag.zip)